Master's Thesis
석사 학위논문

The Study of Thin Film Transistor with Micro Antenna Structure for Wireless Signal Transmission

Jun, Byoung Ok (전 병 옥 田 炳 玉)

Department of Information and Communication Engineering
정보통신융합공학전공

DGIST

2015

Master's Thesis
석사 학위논문

The Study of Thin Film Transistor with Micro Antenna Structure for Wireless Signal Transmission

Jun, Byoung Ok (전 병 옥 田 炳 玉)

Department of Information and Communication Engineering

정보통신융합공학전공

DGIST

2015

The Study of Thin Film Transistor with Micro Antenna Structure for Wireless Signal Transmission

Advisor   :   Professor Jae Eun Jang

Co-advisor :   Professor Hongsoo Choi

By

Jun, Byoung Ok

Department of Information and Communication Engineering

DGIST

A thesis submitted to the faculty of DGIST in partial fulfillment of the requirements for the degree of Master of Science in the Department of Information and Communication Engineering. The study was conducted in accordance with Code of Research Ethics[1]

1(month). 5(day). 2015(year)

Approved by

Professor 장 재 은 (Signature)
(Advisor)

Professor 최 홍 수 (Signature)
(Co-Advisor)

The Study of Thin Film Transistor with Micro Antenna Structure for Wireless Signal Transmission

Jun, Byoung Ok

Accepted in partial fulfillment of the requirements for the degree of Master of Science.

1(month). 5(day). 2015(year)

Head of Committee＿＿장 재 은＿＿(인)
Prof. Jae Eun Jang
Committee Member＿＿최 홍 수＿＿(인)
Prof. Hongsoo Choi
Committee Member＿＿최 지 웅＿＿(인)
Prof. Ji-Woong Choi

ABSTRACT

Wearable and flexible devices have been widely studied. In the flexible display system, thin film transistors (TFTs) are applied as an important building block such like electrical switch, rectifier or amplifier due to its relatively lower process temperature than field effect transistor using single crystal material. Wire connection is employed to supply an electrical power or a driving signal to TFTs. However, the contact electrodes, generally formed by metal thin film, is one of the weakest part, so that it is easily broken in bending or folding situation, since the electrode shape is narrow (~ um level) and long (cm ~ m level) in a row or a column direction. Wireless power and signal transfer (WPST) can be a good candidate to solve this problem. Therefore, wireless thin film transistor (TFT) structure has been studied to apply to various flexible or wearable devices. One of the enabling technologies is the near-field magnetic induction coupling [1]. To apply the WPST connection system to TFT for the flexible system, it is essential to realize a receiving antenna with micro-meter level size structure to withstand the bending situation. The side effect of this micro size antenna is the decrease of transmission efficiency as scaling down the size of antenna. To compensate this side effect for employing micro antenna structure to TFT, the magnetic core (MC) is added to the micro antenna structure to increase the magnetic flux without the size change of antenna structure due to the decrease of the power efficiency as the scale down of antenna size. The MC is consisted of zinc oxide nano-wires (ZnO NWs) and nikel (Ni), a ferromagnetic material, which is coated on the vertical ZnO NWs. Due to the increase of self-resonance frequency with decreasing antenna size, we chose an amorphous indium gallium zinc oxide (a-IGZO) TFT, which showed higher mobility than a-Si TFT and optimized the TFT structure for high frequency driving. Then, WPST system is adopted to the a-IGZO TFT and the charancteristics are analyzed. To improve the wireless a-IGZO TFT sysem, various MC structures and a-IGZO TFT designs are studied and applicability of wireless TFT is estimated for the flexible and wearable system in this paper.

Keywords: Wireless power transmission, A-IGZO TFT, Wireless TFT

List of contents

List of tables

List of figures

I. **INTRODUCTION**

1.1 Motivation

Currently, wearable and flexible devices have been widely studied. In the flexible device system, TFTs are applied as an important building block such like electrical switch, rectifier or amplifier due to its relatively lower process temperature than field effect transistor using single crystal material. Wire connection is employed to supply an electrical power or a driving signal to TFTs. However, the contact electrodes, generally formed by metal thin film, is one of the weakest part, so that it is easily broken in bending or folding situation, since the electrode shape is narrow (~ um level) and long (cm ~ m level) in a row or a column direction as shown Fig 1.1.1.
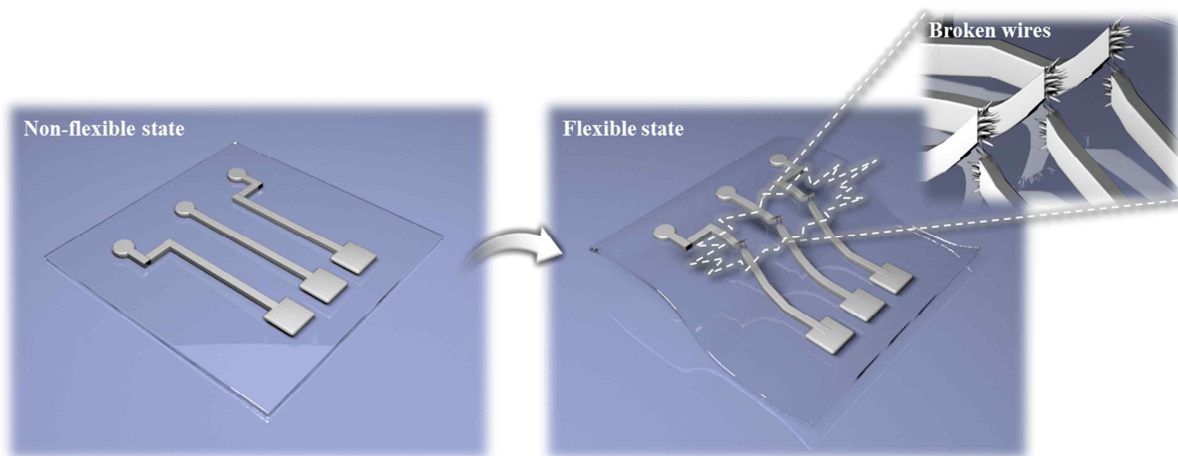
Fig 1.1.1 Conctact electrodes in bending or folding situation.

Several groups have introduced the wire concepts to solve the problem, in the way that the wire can be transformed to tolerate the stress in bending or folding state. Fig 1.1.2 shows the wire concepts, which are two and three dimensional wrinkle wire shapes from J. Rogers research group in University of Illinois [2-3].

(a)   (b)
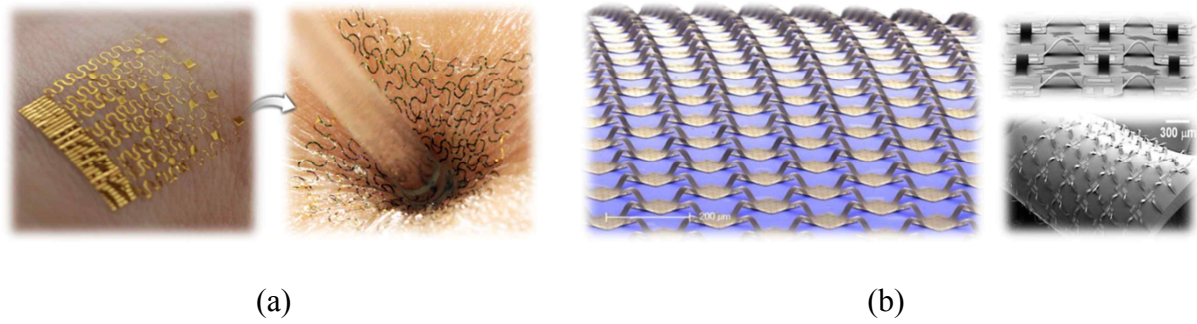
Fig 1.1.2 Wrinkle wire concepts. (a) Two-dimensional wrinkle wire concept. (b) Three-dimensional wrinkle wire concept.

In our concept, we tried to remove the wire, which is the fundamental problem. WPST can be a good candidate for our concept. One of the enabling technologies is the near-field magnetic induction coupling. To realize our concept in the wearable and flexible systems, the TFT needs to be operated wirelessly. For this reason, characteristics of wireless TFT are analyzed in this paper.

1.2 Issues of wireless TFT system

There are two main issues to apply the WPST system to TFT for flexible and wearable system at antenna and TFT parts respectively. At the antenna part, it is essential to realize a receiving antenna with micro-meter level size structure to withstand the bending situation. The side effect of this micro size antenna is the decrease of wireless power transmission (WPT) efficiency at low frequency level because WPT efficiency is maximized at a self-resonant frequency however as the antenna size decreases, the self- resonant frequency increases. Hence, at the TFT part, high mobility of TFT is required to follow the frequency in the micro size antenna structure.

1.3 Issue of antenna for WPT

1.3.1 Background and principle of WPT

WPT is the technology to deliver the electrical energy from a power source to an electrical load without interconnecting wire. Approximately 100 years ago, Nikola Tesla proposed the WPT technology. However, the generated power could not satisfy the user needs. Nearly 100 years after Tesla's proposition, it is now possible to use higher frequency radio waves, or microwaves that satisfy the users. In fact, the WPT is a valuable and convenient technology that can be used to charge the batteries in mobile phone, laptop PC, electric vehicles and other equipment [4]. Among the several WPT technologies, most-used method is an electromagnetic induction coupling. All WPT technologies using electromagnetic induction method are based on Maxell's equations in Eq 1[5].

$$\nabla \times E = -\frac{\partial B}{\partial t}$$

$$\nabla \times H = J + \frac{\partial D}{\partial t}$$

$$\nabla \cdot D = \rho$$

$$\nabla \cdot B = 0 \qquad\qquad (1)\,[5]$$

The first Maxell's equation is from a Faraday's law where 'E' and 'B' are an electric field and a magnetic flux density respectively. The equation represents that when time varying magnetic fields generate around a conducting wire, time varying electric fields are formed in the conducting wire and vice versa as shown Fig 1.3.1.1 (b). The second Maxell's equation is from a Ampere's law where a magnetic field intensity, an electric current density and an electric flux density are expressed as the ornamentation, 'H', 'J' and 'D' respectively. The

equation signifies that when time varying current is applied in a conducting wire, time varying magnetic field is formed around the conducting wire and vice versa in Fig 1.3.1.1 (a).

(a)   (b)
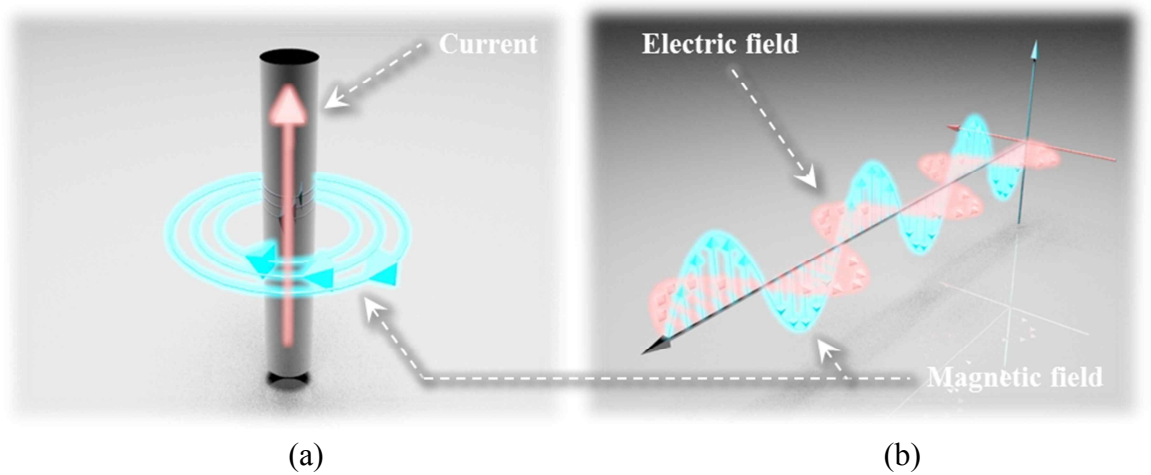
Fig 1.3.1.1 Mechanism of Ampere's and Faraday's law. (a) Mechanism of Ampere's law. (b) Mechanism of Faraday's law.

When the conducting wire has a loop-shaped structure, the magnetic filed can be concentrated in the center of loop and as increasing the number of loops like a coil, the magnetic field is reinforced. Generally, WPT system consists of transmitting (TX) and receiving (RX) antennas and the time varying magnetic field flux propagates a RX in the range of allowable magnetic field generated from TX. In fact, the power can be transferred wirelessly as shown Fig 1.3.1.2.
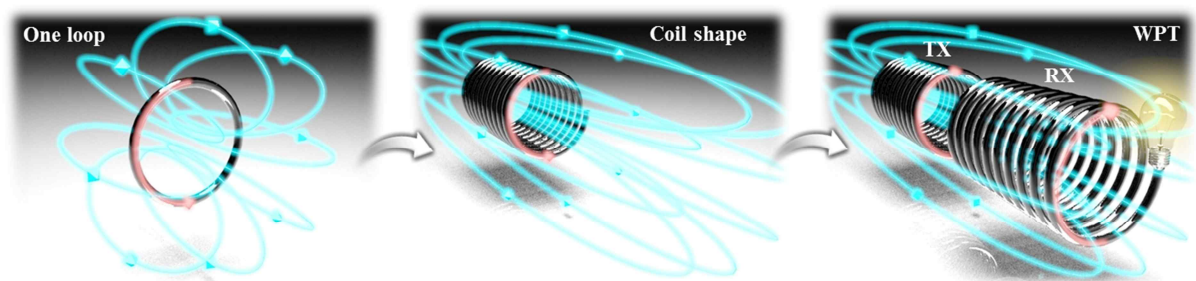
Fig 1.3.1.2 Mechanism of WPT system.

1.3.2 Classification of WPT technologies

All WPT technologies are based on Maxwell's equations. However, the WPTs are subdivided into three major technologies based on inductive, magnetic resonance coupling and electromagnetic (EM) radiation according to differences in their applications. Fistly, WPT is based on inductive coupling as shown in Fig 1.3.2.1 (a). The efficiency of WPT depends on the coupling coefficient, which in turn depends on the distance between two coils. Therefore, the wireless energy cannot be carried over a distance longer than a few millimeters with high efficiency, and the frequency used in inductive coupling is below some dozen megahertz [6]. In fact, available application can be electric toothbrush, charging pad for cell phones and laptops when the charging node and power receiving node are close in contact [7]. Secondly, magnetic resonance coupling WPT is based on the well-known principle of resonance coupling [8]. A resonator is formed by adding capacitance 'C' on an induction 'L' coil as shown in Fig 1.3.2.1 (b). Two resonators are coupled electromagnetically, and the energy in one resonator is transmitted to the other through an evanescent mode wave. This technology was started at 2006 that MIT researchers demonstrated a WPT experiment using resonance coupling [9]. Although the magnetic resonant coupling has great potential with high efficiency over several meters, a number of technical challenges still exist before transitioning this technology to a successful commercial product because this technology has high efficiency only within several-meter range when source and receiving coils are aligned coaxially [7]. The application of this technology can be charging mobile devices, electric vehicles, implantable devices and wireless sensor networks (WSNs). Finally, the WPT is based on EM wave. The EM radiation emits energy from the transmitting antenna of a power source to the receiving antenna via radiative EM waves. Depending on the energy-emitting direction, it can be classified into omnidirectional radiation and unidirectional radiation. Although suitable for transferring information, omnidirectional radiation suffers from a serious efficiency

problem in energy transfer since EM waves decay quickly over distance. Moreover, to prevent potential health hazards to humans from EM radiation, omnidirectional radiation is only appropriate for ultra low-power sensor nodes [8] with very low sensing activities. In fact, this technology is used in charging a WSN for environmental monitoring. When a clear line-of-sight path exists, unidirectional radiation can achieve high power transmission over a much longer distance kilometer-range by using a microwave or laser beam. This concept can be applied to enormous solar power satellite systems as shown in Fig. 1.3.2.1 (c) [10].

| (a) | (b) | (c) |
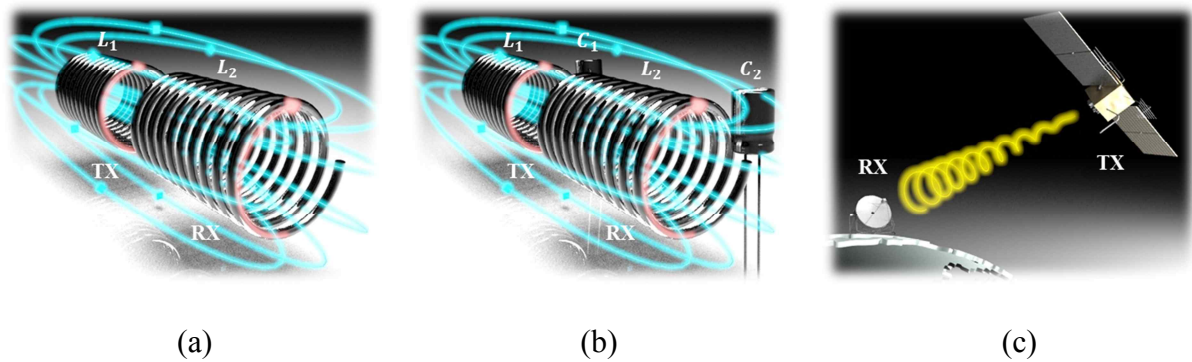
Fig 1.3.2.1 Classification of WPT. (a) Inductive coupling. (b) Magnetic resonance coupling. (c) EM radiation using microwave.

To select the proper WPT technology, characteristic of TFT should be considered which the TFT has cut-off frequency point that input signal is no longer transmitted. Inductive coupling WPT has an advantage which can be used in wide range of frequency hence, this technology is appropriate for our wireless TFT concept.

1.3.3 Issue of spiral coil based on inductive coupling

(a)   (b)
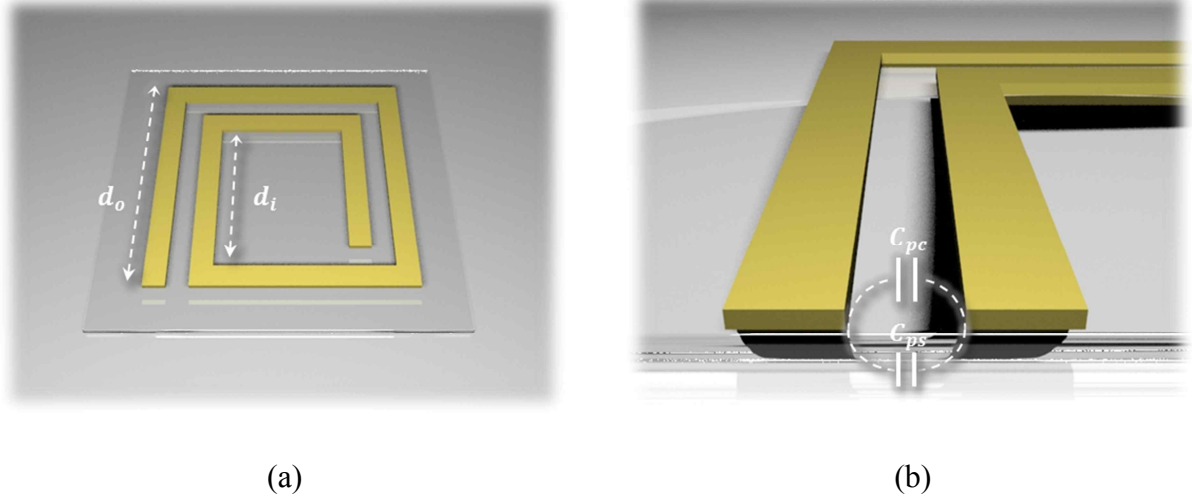
Fig 1.3.3.1 Geometrical parameters of spiral coil. (a) Top view. (b) Cross-section view [11].

Wireless operation of TFT demands much smaller size of receiving antenna. This would require micro-fabrication techniques that result in lithographically defined planar structures. Printed spiral coil offers more flexibility in defining their characteristics, and have the ability to conform on flexible substrates, such as polyimide or parylene [11]. Hence, the flat spiral type coil antenna structure is suitable to realize the wireless TFT system. First equation in Eq 2 shows a formula for inductance 'L' calculation of planar spiral inductors and Fig 1.3.3.1 (a) represents the parameters for the inductance calculation.

$$L = \frac{\mu_0 \cdot n^2 \cdot d_{avg} \cdot a_1}{2} \left[\ln\left(\frac{a_2}{\varphi}\right) + a_3 \cdot \varphi + a_1 \cdot \varphi^2 \right]$$

$$\varphi = \frac{d_o - d_i}{d_o + d_i}$$

$$C_p = C_{pc} + C_{ps}$$

$$d_{avg} = (d_o + d_i)/2 \qquad\qquad (2)\ [18]$$

where 'a_i' are the coefficients depanding on coil shapes as shown in Table 1, 'n' is the number of turns, 'μ_0' is the permeability of free space, 'd_o' and 'd_i' are the outer and inner diameters of coil, respectively [12].

TABLE I.   Coefficients for current sheet expression [11]

Layout	a_1	a_2	a_3	a_4
Square	1.27	2.07	0.18	0.13
Hexagonal	1.09	2.23	0.00	0.17
Octagonal	1.07	2.29	0.00	0.19
Circle	1.00	2.46	0.00	0.20

Second equation in Eq 2 represents the parameter known as fill factor 'φ', which changes from 0, when all turns are concentrated on the perimeter like filament coils, to 1, when the turns spiral all the way to the center of the coil [11]. Third equation in Eq 2 shows a parallel parasitic capacitance 'C_p' between the spiral conductor sidewalls shown in Fig 1.3.3.1 (b). Fourth equation in Eq. 2 signifies an average diameter 'd_{avg}' according to the 'd_o' and 'd_i'. From Eq 2, we can confirm that declining the size of spiral coil causes to deteriorate the inductance value and raise self-resonant frequency '$f_{sr} = 1/2\pi\sqrt{L \cdot C_p}$' up, which is the point with highest power transmission efficiency. The WPT efficiency, which is proportional to a quality factor '$Q = (2\pi f \cdot L)/R_p$', can be increased by reducing coil parasitic resistance 'R_p' and increasing the 'L' at an operating frequency 'f'. The 'L' can be improved by the 'n' in coils however, when increasing the 'n', it also affects the coil parasitic resistance so the proper value of the 'φ' needs to be found [13]. However, the 'n' and the 'φ' are limited by lithographic micro-fabrication technique. Hence, the advanced solution is necessary.

1.3.4 Effect of MC

The presence of a high-permeability magnetic material in center of the inductor increases the inductance by providing a low-reluctance path for the flux lines [14]. In the presence of an external applied magnetic flux, The total magnetic flux density 'B_{total}' is given by Eq 3, which is represented as the sum of magnetic flux densites at air core 'B_{air}' and MC 'B_i' where 'H' and 'μ_r' are the magnetic flux and relative permeability of magnetic material. Fig 1.3.4.1 shows the effect of MC presence [15].

$$B_{total} = B_{air} + B_i = \mu_r \mu_0 H = \mu H \qquad \text{(3) [15]}$$

The simplified inductance equation of inductor with the MC can be expressed as Eq 4.

$$L = \frac{\mu_r \mu_0 A_C N^2}{l_c} = L_o + L_{\chi_m}$$

$$L_o = \frac{\mu_0 A_C N^2}{l_c}$$

$$L_{\chi_m} = \frac{(\mu_r - 1)\mu_0 A_C N^2}{l_c}$$

$$\text{(4) [15]}$$

where 'A_C', 'L_o' and 'L_{χ_m}' are the cross-sectional area of core, inductance of air-core inductor and inductance due to presence of MC respectively [15]. In fact, The presence of a high-permeability magnetic material can be good solution to overcome the size-effect as increasing the inductance value of coil.

(a)　　　　　　　　　　　　　　　　　　　(b)
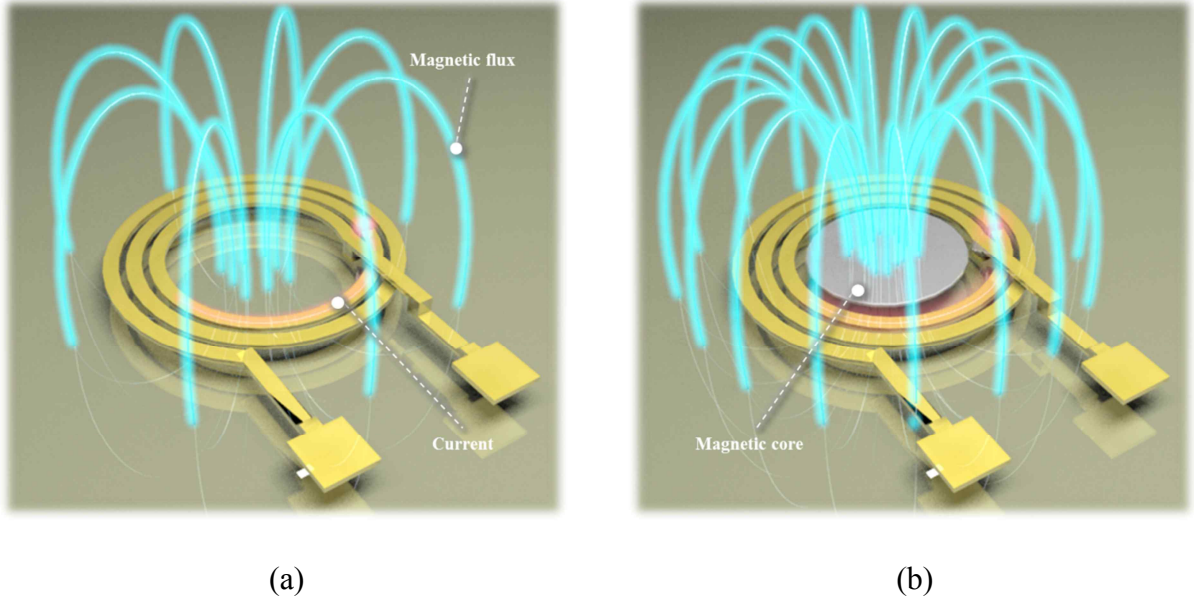
Fig 1.3.4.1 Schematic diagrams for effect of MC. (a) Absence of MC. (b) Presence of MC.

1.3.5 Designs of MC

(a)　　　　　　　　　　　　　　　　　　　(b)
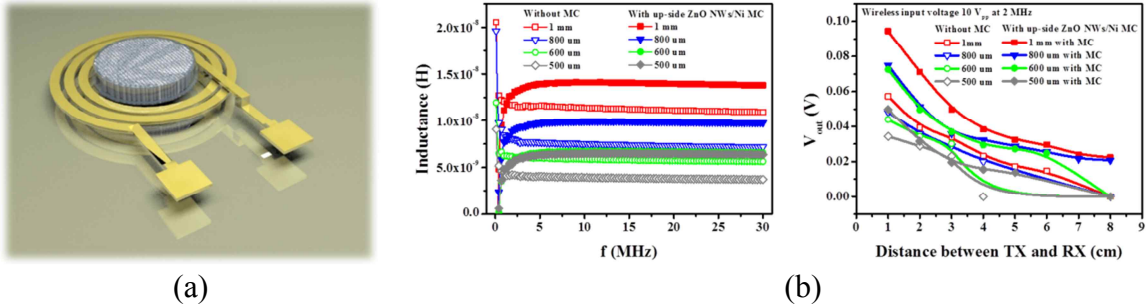
Fig 1.3.5.1 Structure of up-side ZnO NWs/ Ni MC and characteristics. (a) Up-side MC structure with ZnO NWs/Ni. (b) Inductance and WPT effciency of coils with and without up-side MC with ZnO NWs/Ni.

When the MC is composed of the ferro-magnetic material, it can help to focus the magnetic field more in the center of the flat spiral coil and to reduce the loss of magnetic fields escaping from the center. To enhance the focusing effect with directionality of magnetic flux and increase of effective area in the MC, a vertical three dimensional (3D) structure can be added. In our previous work, we proved that Ni MC assisted by ZnO NWs

could improve the size effect of micro spiral antenna as shown in Fig 1.3.5.1. To improve the performance of MC more, we designed three core structures more. Firstly, bare Ni MCs are added. They includes the up-side and back-side MC structures as shown in Fig 1.3.5.2 (a) and (b), which the back side MC is located by SiO_2 at the position lower than the up-side MC structure on the basis of coil as shown in Fig 1.3.5.2 (d) and (e). Secondly, backside ZnO NWs/Ni core was realized as shown in Fig 1.3.5.2 (c). Several researches support that back side MC structure can enhance the inductance value and WPT efficiency [16-19].

(a)   (b)   (c)

(d)   (e)

Fig 1.3.5.2 Schematic diagrams of MCs classification. (a) Up-side MC structure with Ni. (b) Back-side MC structure with Ni. (c) Back-side MC structure with ZnO NWs/Ni. (d) Cross-section view of up-side MC structure with ZnO NWs/Ni. (e) Cross-section view of back-side MC structure with ZnO NWs/Ni.

1.4 Issues of amorphous oxide semiconductor (AOS) TFTs
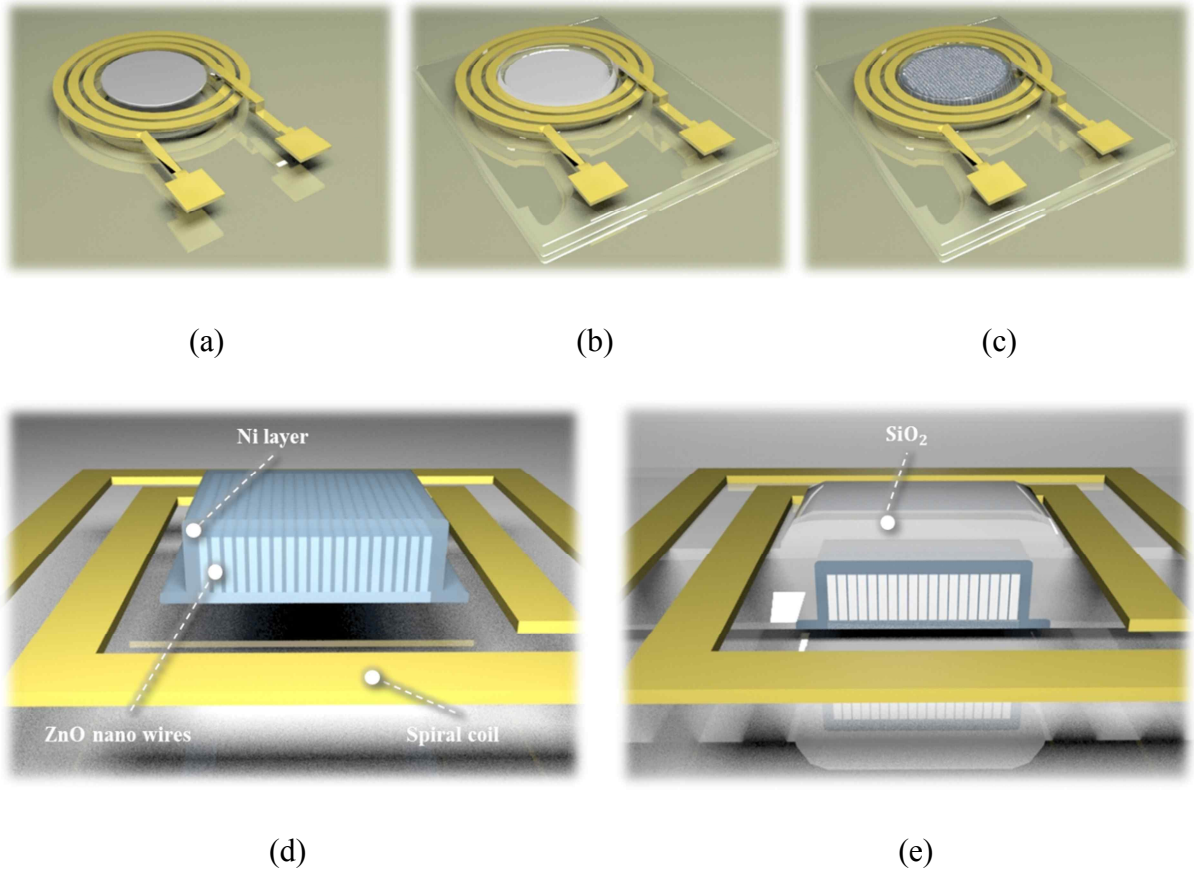
1.4.1 Background and principles of AOS TFTs

A-Si:H is the material that is most widely investigated for flexible electronics and has been demonstrated to be useful in developing flexible TFTs [20]. However, device performances and applications are limited by the properties inherent to this material. The field-effect mobilities 'μ_{FE}' of α-Si:H TFTs are only < 2 cm$^2 \cdot$ V$^{-1} \cdot$ s^{-1}. These values are not satisfactory for high-resolution carrier injection devices such as electroluminescence (OEL) displays. Therefore, larger-mobility amorphous materials that can be formed at low temperatures have been sought. Recently, AOSs have reported that the materials have much more suitable properties for developing flexible TFTs than conventional amorphous semiconductors (α-SCs) [21]. AOS-based TFTs fabricated at room temperature (RT) exhibited 'μ_{FE}' of 6~9 cm$^2 \cdot$ V$^{-1} \cdot$ s^{-1}, which are almost one order of magnitude higher than those reported for a-Si:H and organic TFTs [20]. In 2003, AOSs ZnO-Rh$_2$O$_3$ were found as first P-type AOS and PN-junction diodes with a good performance were fabricated at low temperature by use of this material and N-type α-InGaZnO$_4$ (α-IGZO). In 2004, TFTs, using α-IGZO as the channel, were fabricated on plastic (PET) substrates and the resulting TFT exhibited a 'μ_{FE}' of > 10 cm$^2 \cdot$ V$^{-1} \cdot$ s^{-1} even in a bent state [21].

1.4.2 Issues of AOS TFT

Electrical characteristics of AOS TFT can be divided into two parts, which are DC characteristic and AC response. Firstly, the DC electrical characteristics of TFT devices are represented by the 'μ_{FE}' and threshold voltage 'V_{th}'. Such parameters strongly depend on the device structure and fabrication process, the AOS materials, and the gate dielectrics or interconnect metals in contact with the semiconductor. Because fast switching is the key role of TFT devices in electronic applications, one would in general target, high 'μ_{FE}'

values and 'V_{th}' does to zero as small as possible [22]. The operation of a field-effect transistor can be divided by two regime, which are linear and saturation regimes. In the linear regime, Eq 5 describes the current-voltage characteristics, in which the current increases linearly with source-drain voltage 'V_{DS}'.

$$I_{DS(\hbar\ )} = \frac{\mu_{FE}WC_i}{L}V_{DS}(V_{GS} - V_{th}), \qquad \text{for } V_{DS} \ll V_{GS} - V_{th} \qquad \text{(5) [22]}$$

where 'W' is the channel width, 'L' is the channel length, 'C_i' is the capacitance per unit area of the gate insulator as shown in Fig 1.4.2.1, '$I_{DS(\hbar\ )}$' is the drain-to-source current and 'V_{GS}' is the gate voltage in linear regime.
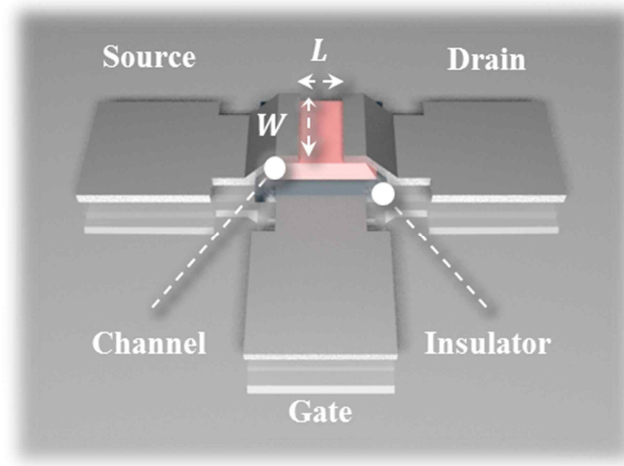

Fig 1.4.2.1 Geometrical parameters of AOS TFT.

The linear regime '$\mu_{FE(\hbar\ )}$' is derived from the slope of an experimentally measured '$I_{DS} - V_{GS}$' transfer characteristic using Eq 6.

$$\mu_{FE(\hbar\ )} = \frac{L}{WC_iV_{DS}}\frac{\partial I_{DS}}{\partial V_{GS}} \qquad \text{(6) [22]}$$

In the saturation regime, the current saturates at '$I_{DS(sat)}$' as given by Eq 7.

$$I_{DS(sat)} = \frac{\mu_{FE} W C_i (V_{GS} - V_{th})^2}{2L} = \frac{\mu_{FE} W C_i V_{DS(sat)}^2}{2L},$$

$$\text{for } V_{DS} = V_{GS} - V_{th} = V_{DS(sat)} \qquad \text{(7) [22]}$$

In the saturation, the current increases quadratically with '$V_{GS} - V_{th}$' because the inversion charge increases by this amount, as does the maximum potential drop along, the channel. The Eq 8 gives the saturation regime '$\mu_{FE(sat)}$'.

$$\mu_{FE(sat)} = \frac{2L}{W C_i} \left(\frac{\partial \sqrt{I_{DS}}}{\partial V_{GS}} \right)^2 \qquad \text{(8) [22]}$$

Secondly, the AC response of TFT devices are represented by the current-gain cutoff frequency 'f_{max}' in metal-oxide-semiconductor (MOS) transistors, which is used to evaluate dynamic performance. When looking into the input port between the gate and source, there are capacitors at high-frequency as shown Fig 1.4.2.2. However, the capacitor behaves like an open circuit at low-frequency. Therefore, it is standard practice to model the low-frequency input to the MOS transistors by an open circuit. At the output port, the DC drain current was described to be a function of 'V_{DS}' and 'V_{GS}', which is '$I_{DS} = I_{DS}(V_{DS}, V_{GS})$'. When AC drain and gate potential, 'v_{ds}' and 'v_{gs}', are respectively added to the DC drain and gate terminal voltages, 'V_{DS}' and 'V_{GS}', the drain current through the structure is modified to '$I_{DS}(V_{DS}, V_{GS}) + i_{ds}$', where '$i_{ds}$' is the AC component of the drain current. Given the small-signal equivalent circuit of Fig 1.4.2.2, it is possible to estimate the maximum operating frequency or cutoff frequency of an MOS transistor, which are no longer amplifying the input signal under optimum conditions and absolute value of the output current to input current ratio is unity when the output of the transistor is shorted-circuited [22].
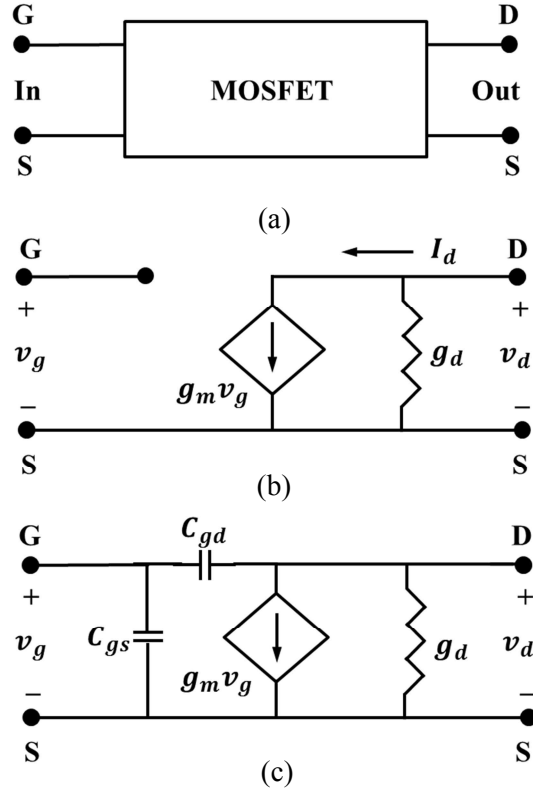
Fig 1.4.2.2 MOSFET equivalent circuits. (a) Two-port network. (b) Low-frequency small-signal model. (c) High-frequency small-signal model [22].

When input AC voltage 'v_{gs}', which is applied to the gate electrode of a MOS transistor, the input AC current with the output shorted-circuited is written as Eq 9.

$$i_{in} = j\omega \left(C_{gs} + C_{gd}\right)v_{gs} \approx j\omega C_i v_{gs}, \qquad \text{for } j = \sqrt{-1} \qquad (9)\,[22]$$

Where the capacitance of gate-drain 'C_{gd}' is taken to be small and the capacitance of gate-source '$C_{gs} \approx C_i$'. Likewise, , the output AC current in the saturation regime of the transistor is given by Eq 10.

$$i_{out} = \mu_{FE(sat)} C_i \frac{W}{L} |V_{GS} - V_{th}| v_{gs} \qquad (10)\,[22]$$

Thus, when setting '$|i_{out}/i_{in}| = 1$', '$f = f_{max}$' can be defined as Eq 11.

$$f_{max} = \frac{\mu_{FE(sat)}|V_{GS} - V_{th}|}{2\pi L^2} = \frac{\mu_{FE(sat)}V_{DS}}{2\pi L^2} \qquad (11)\,[22]$$

The important point to note is that 'L' and '$\mu_{FE(sat)}$' are the key parameters in determining 'f_{max}' [22]. Hence AOS channel material with the higher '$\mu_{FE(sat)}$' should be found.

1.4.3 Effect of IGZO TFT

α-IGZO is a semiconducting material, consisting of indium (In), gallium (Ga), zinc (Zn) and oxygen (O). The α-IGZO has a high 'μ_{FE}' even in the amorphous phase because the carrier transport paths are primarily composed of spatially spread metal ns orbitals with isotropic shape [23]. The 'μ_{FE}' in channel material of TFT is related to its chemical bonding. In crystalline silicon, the carrier transport paths, which comprised of anisotropic sp^3 orbitals and covalent bonding, are strongly directive, hence, amorphous silicon structures are altered by significant changes in bonding angles. This results causes that the carrier transport is degraded. In the case of oxide semiconductor, the phenomenon is completely different from the covalent semiconductors, which conduction band minimum consists of the large spherical isotropic ns orbitals of the metallic cations, where n is the principal quantum number, and direct overlap among the neighbouring metal ns orbitals is possible. When the radii of these orbitals formed larger than the inter-cation distance, which can be achieved for n > 4, the neighboring orbitals always overlap, despite the degree of disorder of the material as shown in Fig 1.4.3.1.

Covalent semiconductors

Crystalline
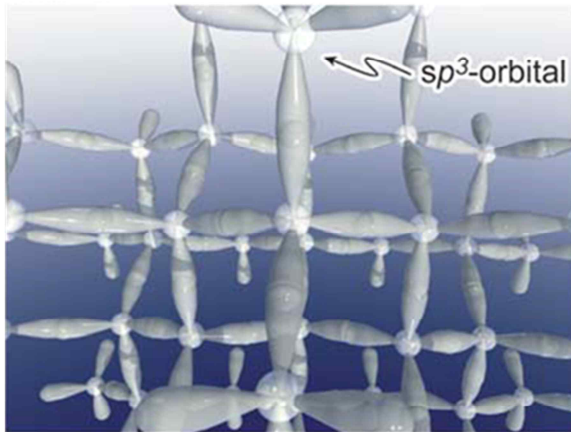
sp^3-orbital

Amorphous

Post-transition-metal oxide semiconductors

Crystalline

Oxygen 2p-orbital

Metal ns-orbital
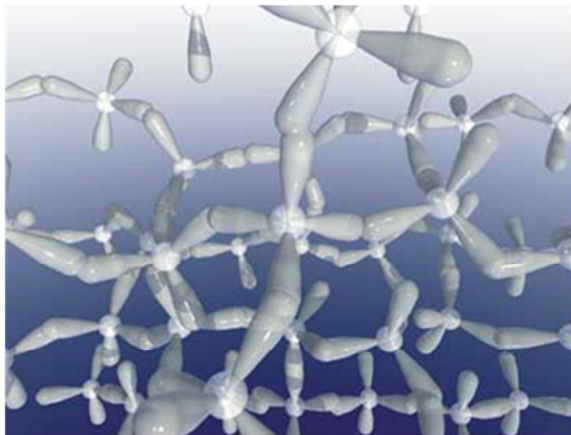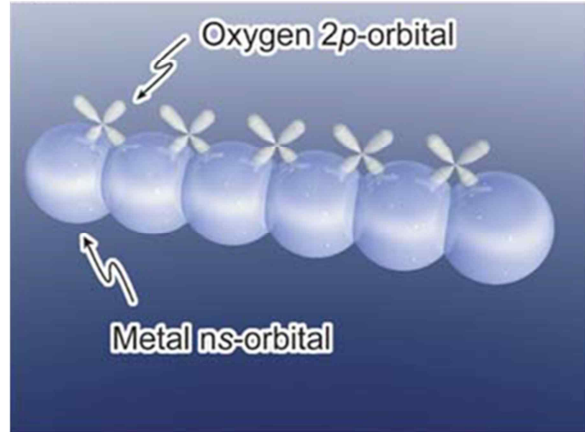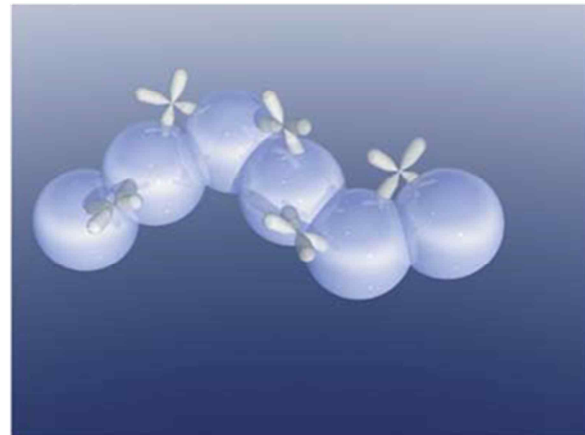
Amorphous

(a)   (b)

Fig 1.4.3.1 Schematic orbital drawings for carrier transport path. (a) Covalent semiconductors. (b)

Post-transition-metal oxide semiconductors [24].

This means that even in the amorphous state, oxide semiconductors always have a well defined carrier path in the conduction band minimum and large 'μ_{FE}' can be achieved [24]. As a result, IGZO-TFT can improve the '$f_{m\,ax}$', It is thus considered to be one of the most promising TFT for use in the wireless system of our concept.

II. **EXPERIMENT DETAILS**

2.1 Fabrication of the micro coil

Circular flat spiral type coils were adopted and glass substrate was utilized to reduce the loss of current into the substrate. To fabricate various designs of micro-devices using photolithography process, photo-mask composed of sodalime and chrome, was designed by using the My CAD program. Before coating the photoresist (PR) (AZ GXR-601), which is positive type, Hexamethldisiloxane (HMDS) was treated to enhance the adhesion between the PR and substrate, then, the PR was spin-coated on a glass substrate with about thickness of 2 um. The thickness of PR depends on the spin-speed, which represented as the revolution per minute (rpm). We used 1000 rpm to form the 2 um thick PR. After coating the PR, the coated substrate was baked on a hot plate about 100 ℃ for 2 minutes for hardening the PR.

The PR was exposed by ultraviolet ray (UV) with 51.8 mJ/cm^2 through the coil patterns in photo-mask and the polymer chains looslely bound by UV exposure in PR were developed by dipping in AZ-developer for 1 minute and 30 second. After developing, the samples were rinsed by deionized (DI) water and dried by blowing N2 gas. The conductor traces of coil with the 500 nm thick gold (Au) on 50 nm thick titanium (Ti) were deposited by using a radio frequency (RF) magnetron sputtering system at an input power of 200 W and pressure of 5 mTorr. The Ti layer was added to enhance the adhesion between the glass substrate and the Au layer. Finally, the printed micro-spiral coils were obtained through the lift-off process, which the PR is removed by dipping in acetone and isopropyl alcohol (IPA) at ultrasonic condition as shown in Fig 2.1.1.
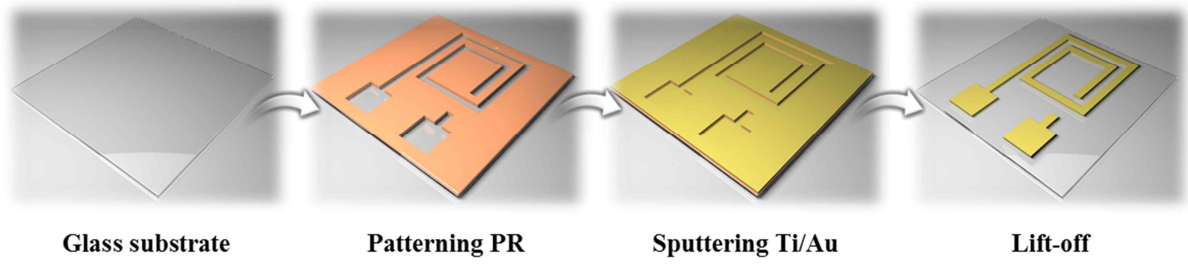
Fig 2.1.1 Fabrication process of micro flat spiral coil antenna.

The 'd_o' of fabricated spiral coil are 500 um and 1 mm. Their parameters are fixed at the 1 turn of number of turns 'n', the 500 nm of thickness 't' , the 80 um of width 'w', the 20 um of spacing 's' between the conductor traces. Fig 2.1.2 shows the optical and scanning electron microscope (SEM) images of micro flat spiral coil antenna.

(a)   (b)
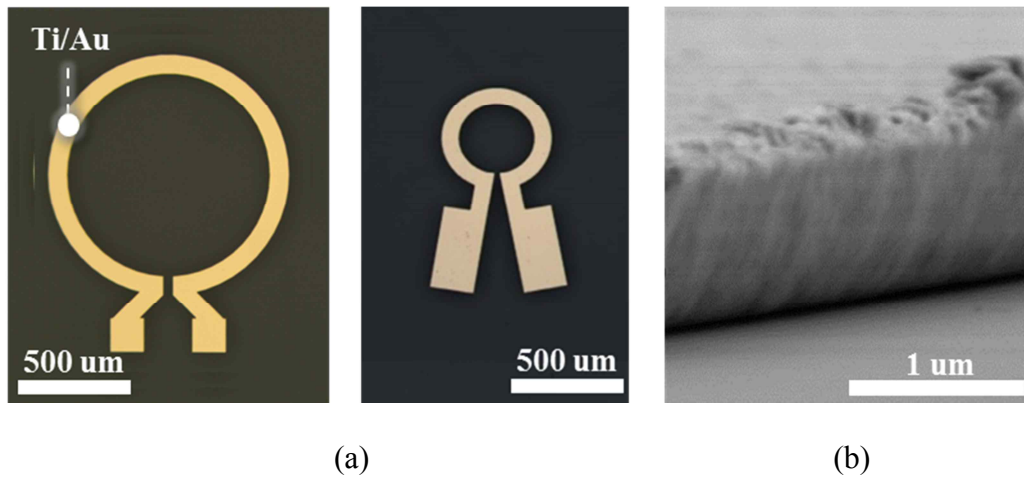
Fig 2.1.2 Structures of micro flat spiral coil antennas. (a) Optical images of micro flat spiral coil antennas. (b) SEM cross-section image of coil trace.

2.2 Fabrication of MC structures

MC structures were added in center of coil antennas. The MC designs are broadly classified by two systems, which are up and back side MC systems. The up-side MC structures are located in same phase with the micro spiral coil and the back-side MC structures are

located under phase than the micro spiral coils. Firstly, two types of up-side MC structures were fabricated after forming the coil, which one is Ni MC structure and another one is MC structure consisted of ZnO NWs and a Ni layer. The ZnO NWs served as frame to coat the Ni layer. After forming the flat spiral coil, the 50 nm ZnO seed layer was patterned by using the RF magnetron sputtering system and a photolithography process in the center of coil loop. After lift-off process of the ZnO seed layer, we used the hydrothermal process which is possible to grow uniformly ZnO NWs on the substrate [25-27]. The sample was suspended upside down direction using plastic tools and was then dipped in a glass bottle filled with 20 mM solution which was mixed by hexamethylenetetramine and zinc nitrate hexahydrate as shown in Fig 2.2.1.

$$(CH_2)_6N_4 + 6H_2O \leftrightarrow 4NH_3 + 6HCHO$$

$$NH_3 + H_2O \leftrightarrow NH_3 \cdot H_2O$$

$$NH_3 \cdot H_2O \leftrightarrow NH_4^+ + OH^-$$

$$Zn^{2+} + 2OH^- \leftrightarrow Zn(OH)_2$$

$$Zn(OH)_2 \rightarrow ZnO + H_2O \qquad (12) [34]$$
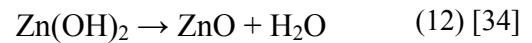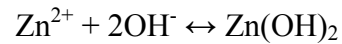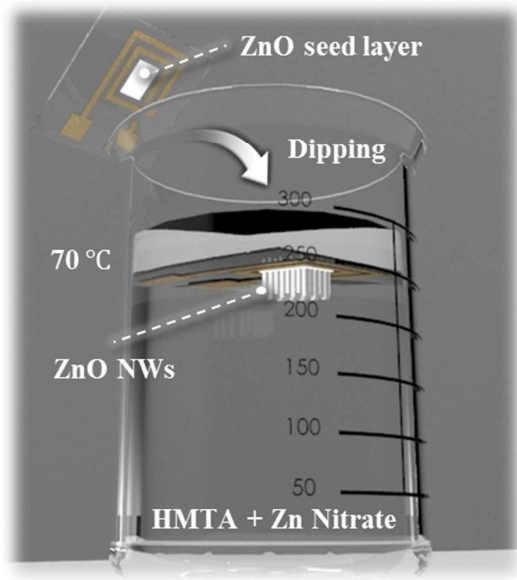
Fig 2.2.1 Process of growing ZnO nano wires.

The nutrient solution was composed of a 1:1 ration of zinc nitrate hexahydrate and hexamethylenetetramine (HMTA). Zinc nitrate salt provides Zn^{2+} ions required for building up ZnO NWs. Water molecules in the solution provide O_2^- ions. The glass bottle was heated in a vacuum oven at 70 ℃ for 48 hours. The grown ZnO NWs were rinsed with an IPA so-

lution to clean the surface of the sample. Then the Ni layer was coated on the vertical ZnO NWs by photolithography, the sputtering and the lift-off process. Fig 2.2.2 shows the fabrication process of up-side MC with ZnO NWs/Ni in the center of micro spiral coil.
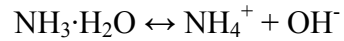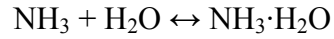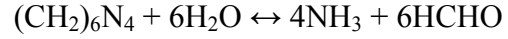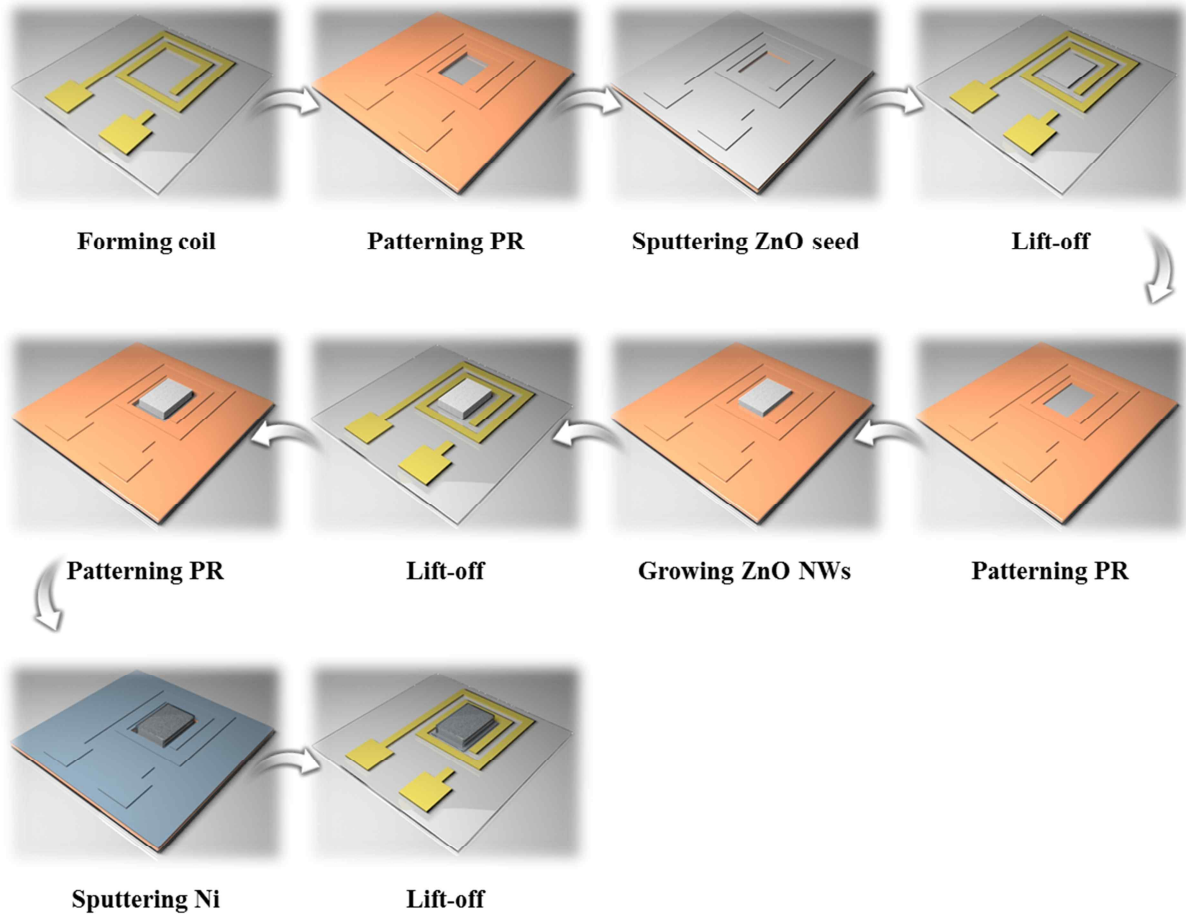

Fig 2.2.2 Fabrication process of coil with up-side ZnO NWs/Ni MC.

Fig 2.2.3 (a-d) show the schematic diagram, optical and SEM images of up-side MC after fabrication. The measurement of X-ray diffraction (XRD) and photo-luminescence (PL) spectrum are the preferred orientation of ZnO NWs [28-29]. The measurement show that ZnO NWs are formed as a single crystal as given by Fig 2.2.3 (e-f).
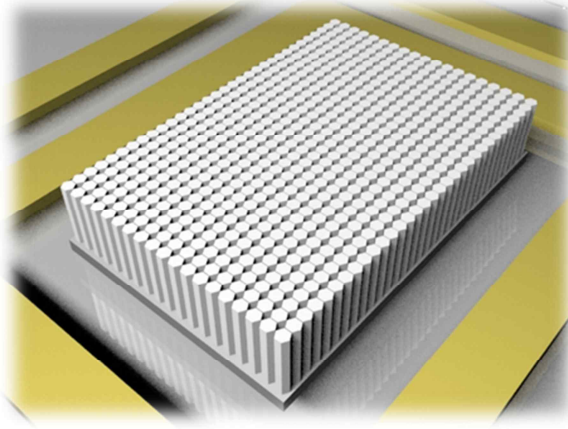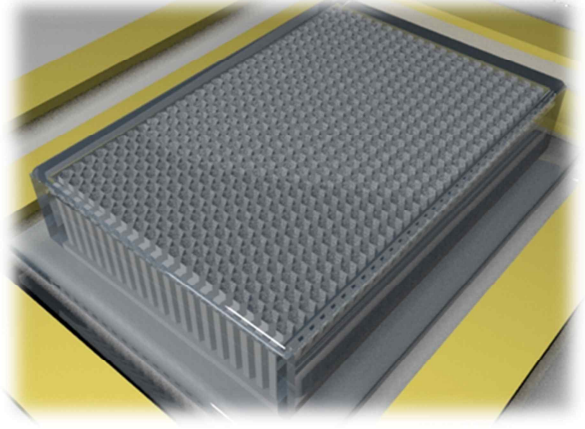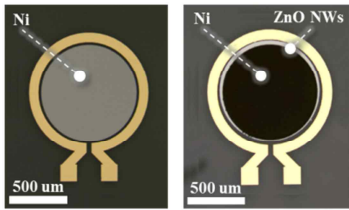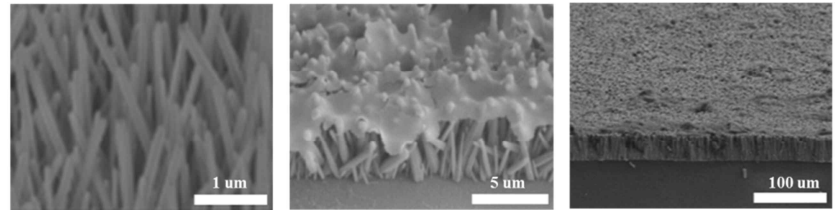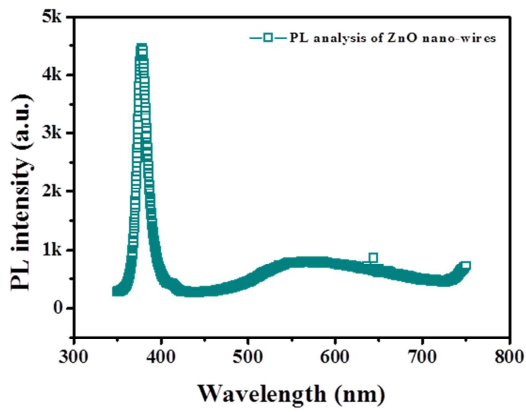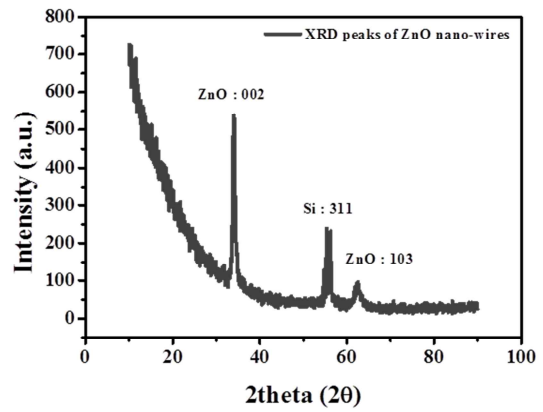
Fig 2.2.3 Structures and properties of up-side ZnO NWs/Ni MC. (a) Schematic diagram of ZnO NWs in the center of spiral coil. (b) Schematic diagram of Ni pattern coated on ZnO NWs in the center of spiral coil. (c) Optical images of spiral coils with up-side Ni and ZnO NWs/Ni MC. (d) SEM images of ZnO NWs and Ni layer coated on ZnO NWs. (e) PL analysis of ZnO NWs. (c) XRD peaks of ZnO NWs on glass substrate.

Secondly, two types of backside MC structures were fabricated in the same way with above process before patterning the coil, which one is Ni MC and another on is ZnO NWs/Ni MC. After patterning MC structures, about 4 um thick SiO_2 was deposited on the MC structures by a plasma enhanced chemical vapor deposition (PECVD) system, then, micro spiral coils were patterned as the centers of MCs were aligned with the center of coils. Fig 2.2.4 represents the fabrication process of micro spiral coil with back-side MC of ZnO NWs/Ni and Fig 2.2.5 shows the optical and SEM images of fabricated MC.

Forming ZnO NWs/Ni MC   Deposition of SiO_2 Formation of coil

Fig 2.2.4 Fabrication process of back-side ZnO NWs/Ni MC.

(a)   (b)

Fig 2.2.5 Structures of back-side ZnO NWs/Ni MC. (a) Optical images of spiral coils with back-side Ni and ZnO NWs/Ni MC. (b) SEM images of SiO_2 deposited on ZnO NWs/Ni MC in the center of spiral coil.

2.3 Fabrication of α-IGZO TFTs

Fig 2.3.1 Fabrication process of α-IGZO TFT.

The micro flat spiral coil antenna with MC and α-IGZO TFTs were fully fabricated at low temperature, because it is prerequisite to realize the flexible system. A glass was used as a substrate and the gate electrode, 150 nm thick aluminum (Al) was patterned by using RF magnetron sputtering system and photolithography process. The 200 nm thick SiO_2 gate insulator was deposited by PECVD and formed by using reactive ion etching system with fluoro carbon gas CF_4 and CHF_3. After that, the active layer of the 80 nm thick α-IGZO ($InGaZnO_4$ target) semiconductor was sputtered by the RF magnetron sputtering sys-

tem at a gas mixing ratio of Ar/O$_2$= 50/5 (sccm/sccm), and at input power of 400 W and pressure of 5 mTorr, respectively. Then, the α-IGZO was wet-etched by using buffered oxide etchant (BOE) 6:1 and annealed at 300 ℃ for 1 hour in ambient oxygen. Finally, using the RF magnetron sputtering system and a photolithography process, the source-drain electrodes were formed with 150 nm thick Al. Al material was used to decrease the resistance at metal-semiconductor contact because Al has a work function similar with α-IGZO material so it can make ohmic contact and high ON current can be obtained, which the material with higher work function than α-IGZO forms schottky contact. Firstly fabricated TFT design has parameters that 'W' is 100 um and 'L' is 40 um and Fig 2.3.1 shows the fabrication process of α-IGZO TFT. To improve the 'μ_{FE}' and '$f_{m\,ax}$' of α-IGZO TFT, we designed α-IGZO with various channel length and thickness, which the channel length was changed from 10 um to 100 um and the channel thickness varies from 5 nm to 40 nm as shown in Fig 2.3.2.
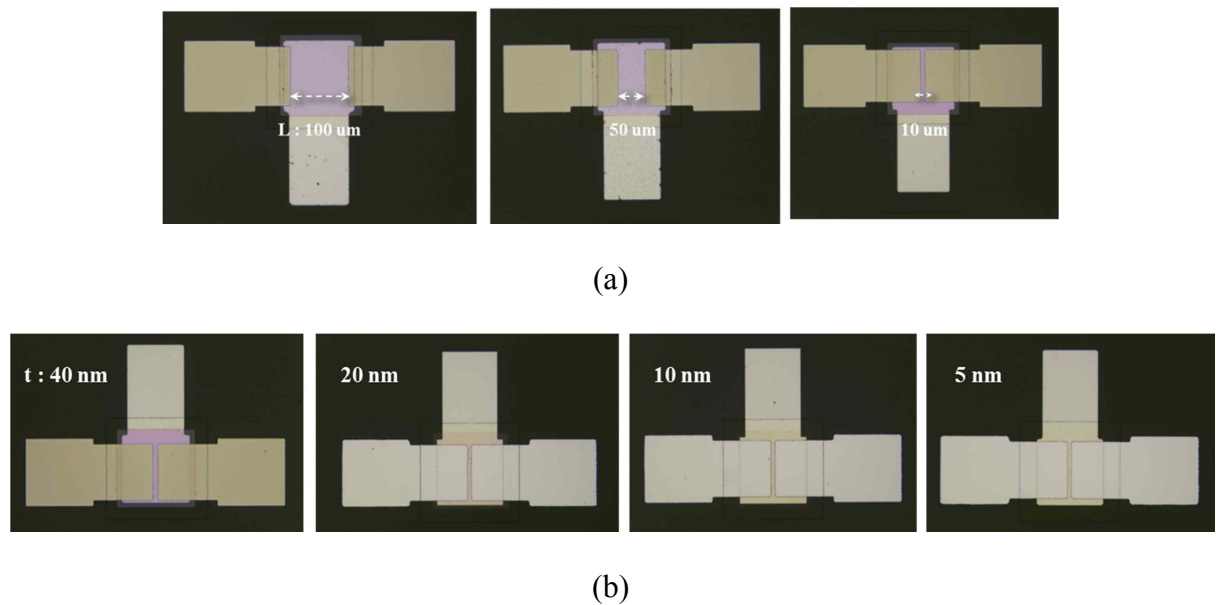

(a)

(b)

Fig 2.3.1 Optical images of α -IGZO TFT. (a) Optical images of α-IGZO TFT with various channel length. (b) Optical images of α-IGZO TFT with various channel thickness.

2.4 Fabrication of wireless α-IGZO TFTs

Firstly, the a-IGZO TFT with '*W*' of 100 um and the '*L*' of 40 um was fabricated at low temperature on the glass substrate. After fabricating the a-IGZO TFT, the flat spiral antenna structure with the 'd_o' of 500 um and the '*n*' of 1 turn was connected with the source-drain electrodes of a-IGZO TFT. Then, the up-side ZnO NWs/Ni MC was patterned. All fabrication were progressed at low temperature, which the fabrication process can reduce damage from heat and the wireless a-IGZO TFT system can be realized on the flexible substrate. Fig 2.4.1 shows the fabrication process of wireless α-IGZO TFT with up-side ZnO NWs/Ni MC.

| Forming α-IGZO TFT | Fabricating spiral coil | Patterning up-side ZnO NWs/Ni MC |
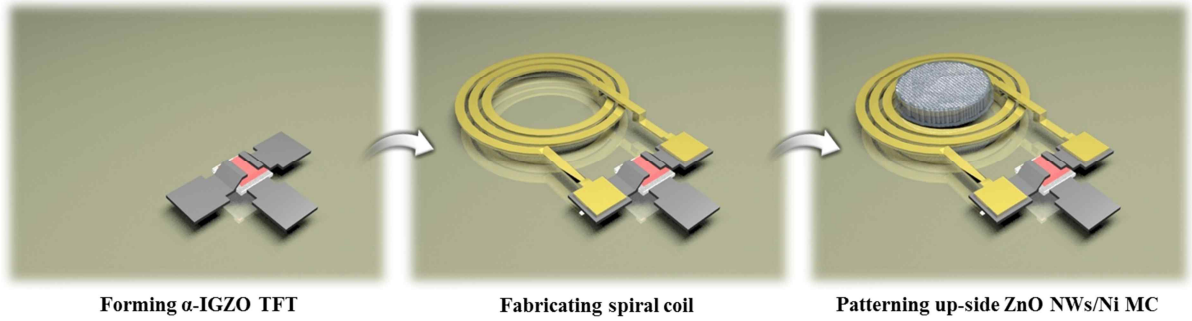
Fig 2.4.1 Fabrication process of wireless α-IGZO TFT with up-side ZnO NWs/Ni MC.

To enhance the performance of wireless α-IGZO TFT, the α-IGZO TFT was formed with the highest cut-off frequency and the threshold voltage close to zero as controlling the channel length and thickness. After then, the back-side ZnO NWs/Ni MC was fabricated after forming the α-IGZO TFT and spiral coil antennas with the 'd_o' of 1 mm were connected with the source-drain and gate electrodes of a-IGZO TFT respectively as shown in Fig 2.4.2.

<div align="center">(a)   (b)</div>

Fig 2.4.2 Structures of wireless α-IGZO TFTs with back-side ZnO NWs/Ni MC. (a) Antenna connected on source-drain electrodes of α-IGZO TFT. (b) Antenna connected on gate-source electrodes of α-IGZO TFT.

2.5 Measurement systems

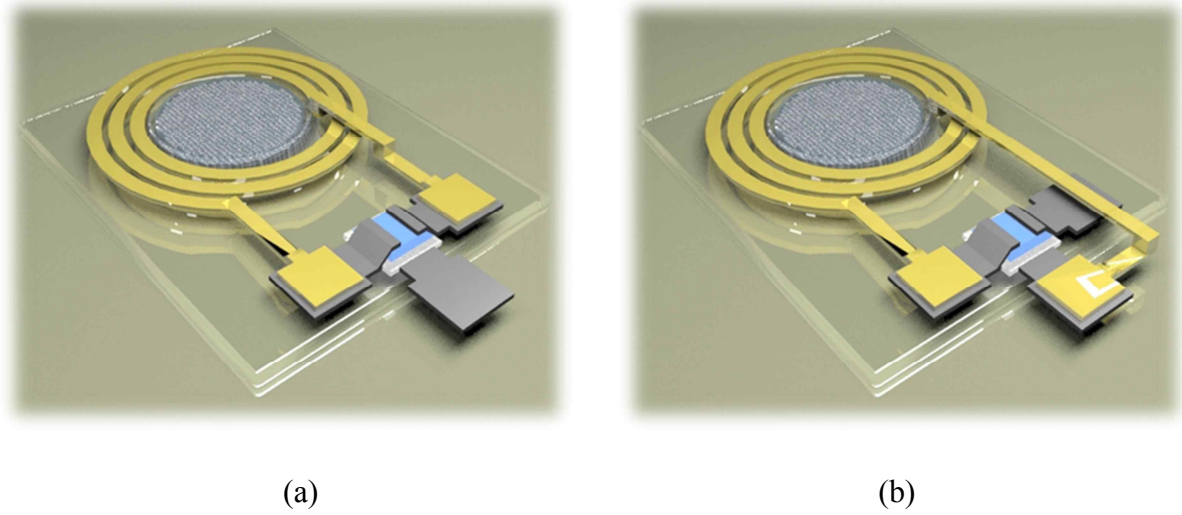The inductance, impedance and s-parameter of antennas were measured by using an impedance analyzer and a network analyzer (Agilent technology E5061B) in Fig 2.5.1 (a). The frequency range was found to be from 100 kHz to 30 MHz. The inner connection pad was connected to a test fixture (Agilent technology 16047E) by using a wire bonding technique where the thickness of the aluminum wire was about 1 mil (25 um). To measure the WPT efficiency, the transmitting part was set by the function generator (Agilent technology 33250A) and the WPT efficiency was measured by digital phosphor oscilloscope (Tektronix DPO3034) in Fig 2.5.1 (b). The DC characteristics of α-IGZO TFTs were measured by Keithley semiconductor analyzer in probe station and the AC characteristics were measured by the probe station connected with function generator, power supply and oscilloscope as shown in Fig. 2.5.1 (c).

(a)

(b)

(c)

Fig 2.5.1 Measurement systems. (a) Measurement system for inductance. (b) Measurement system for WPT efficiency. (c) Measurement system for DC and AC characteristics of α-IGZO TFT.

III. **RESULTS AND DISCUSSION**

3.1 Characteristics of α-IGZO TFT

After forming of α-IGZO TFT, firstly, DC characteristics were measured. Figure 2 and 3 show the DC electrical characteristics of α-IGZO TFT. The electrical characteristic of the TFT was measured using a Keithley semiconductor analyzer by supplying DC 'V_{GS}' and 'V_{DS}'. Fig. 3.1.1 shows the transfer and output curve of fabricated α-IGZO TFT. The measured 'V_{th}' of TFT is about -10V. It can be controlled by thickness of IGZO channel layer [30].

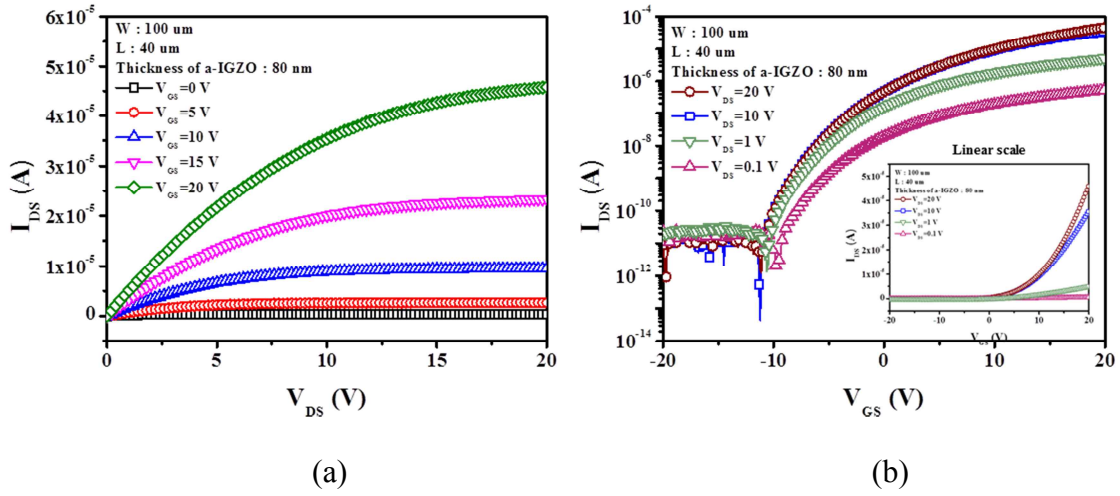

Fig 3.1.1 Output and transfer curve of a-IGZO TFT (a) Output curve of a-IGZO TFT (b) Transfer curve of a-IGZO TFT

The '$\mu_{FE(lin)}, (V_{DS} = 0.1\ V)$' and '$\mu_{FE(sat)}, (V_{DS} = 20\ V)$' were calculated by using the Eq. 26 and 30, where, 'W' is 100 μm, 'L' is 40 μm, and 'C_i' is 17.4 nF. The mobility values were extracted from the linear and saturation regression plots of the transfer curves as shown Fig. 3.1.2. We can confirm that '$\mu_{FE(sat)}$' values in both regions, the decreased according to the decreasing channel length as we previously described. We also found that the field-effect

mobility of a-IGZO TFT in the saturation region was lower than that in the linear region. The decrease in the field effect mobility in the saturation region compared with the linear region is caused by electrode contact resistance and channel length, which, when the channel length is short, the parasitic resistance is increased because the short channel length leads to additional current flow by fringing electrical-field beyond the device edges and side-wall effects associated with source-drain resistance [31]. The measurement of DC characteristics show that the fabricated TFT well operates as a transistor. However, the calculated '$\mu_{FE(h)}$' value is lower than reported value from other research team so it needs to be improved. The '$\mu_{FE(h)}$' value can be improved by controlling 'L', 'W' and 'C_i' extracted from Eq. 26 and 30.

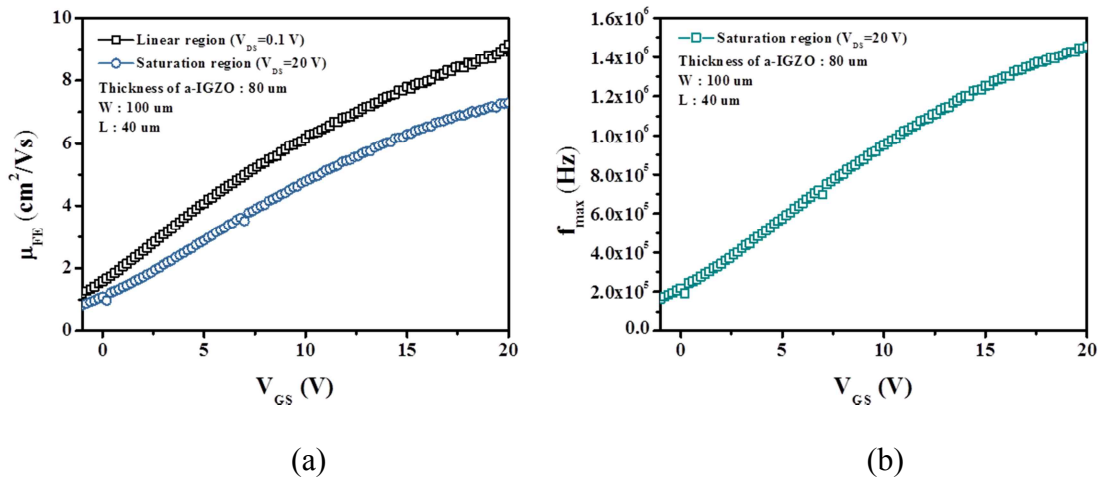(a)   (b)

Fig 3.1.2 Mobility and cutoff frequency. (a) Saturation and linear region mobility according gate voltage. (b) Cutoff frequency according gate voltage.

Secondly, AC characteristics were measured. For alternating current (AC) electrical characteristics of the TFT, the AC signals are well controlled by the gate bias as shown in Fig. 3.1.3. To find a critical frequency of the TFT, the output 'V_{DS}' was measured according to increases of frequency and the characteristics are given by Fig. 3.1.3. As increasing the frequency level,

the output signal becomes decreased and the limit transportation frequency is observed at about 310 kHz, where input DC '$V_{GS} = 1\,V$' and AC '$V_{DS} = 1\,V_{PP}$ (peak-to-peak)'. The limit transportation frequency is related to the '$f_{m\,ax}$', which mainly depends on the mobility and channel length of TFT. Fig. 3.1.3 shows the plotted '$f_{m\,ax}$' values according to the 'V_{GS}' in saturation region of TFT. When the channel length is increased, the field-effect mobility is enhanced however, the '$f_{m\,ax}$' is decreased and it leads to deteriorate the operating frequency. Hence, the critical point should be found.
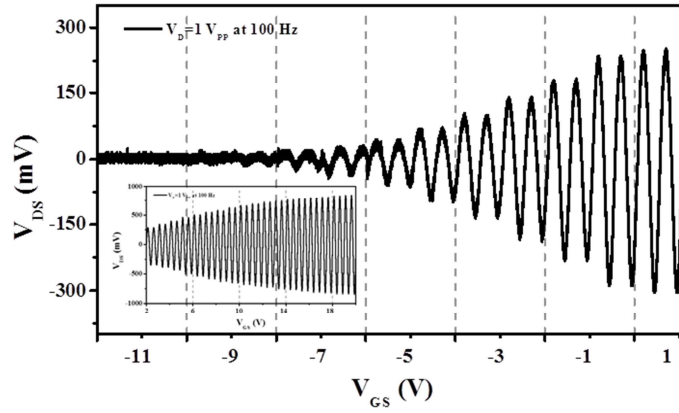
(a)
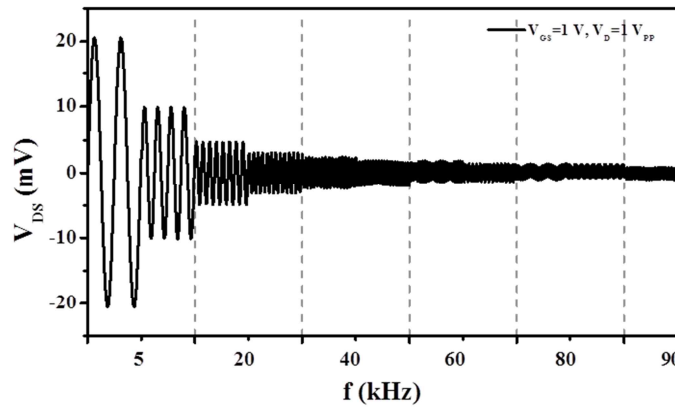
(b)

Fig 3.1.3 AC characteristics of a-IGZO TFT. (a) Output voltage according to gate voltage. (b) Output voltage according frequency sweep.

3.2 Characteristics of wireless source-drain system of α-IGZO TFT

Before optimizing the wireless α-IGZO TFT system, we experimented with the micro spiral coil antenna design with the up-side ZnO NWs/Ni MC and without the MC where the 'd_o' is 500 um and the 'n' is 1 turn from our previous work connected with the source-drain electrodes of α-IGZO TFT with the 'W' of 100 um and 'L' of 40 um to confirm the applicability of micro WPT system into TFT. Fig. 3.3.1 shows the AC characteristics of wireless α-IGZO TFT according to the frequency. The output 'V_{DS}' was measured in the source-drain electrodes of α-IGZO TFT when the power was wirelessly delivered through the TX. The input voltage was supplied to the TX with the 10 V_{PP} by using the function generator and the 20 V of 'V_{GS}' was directly applied to the gate electrode of α-IGZO TFT by DC power supply. The TX of solenoid type coil with macro size wound by 1mm thick copper (Cu) wires was used,which are the 'd_o' of 10 cm and the 'n' of 46 turns and the distance be-tween the TX and the RX was 1 cm. The measured 'f_{sr}' of TX and RX were observed in the range of MHz and GHz respectively as shown in Fig 3.2.1.
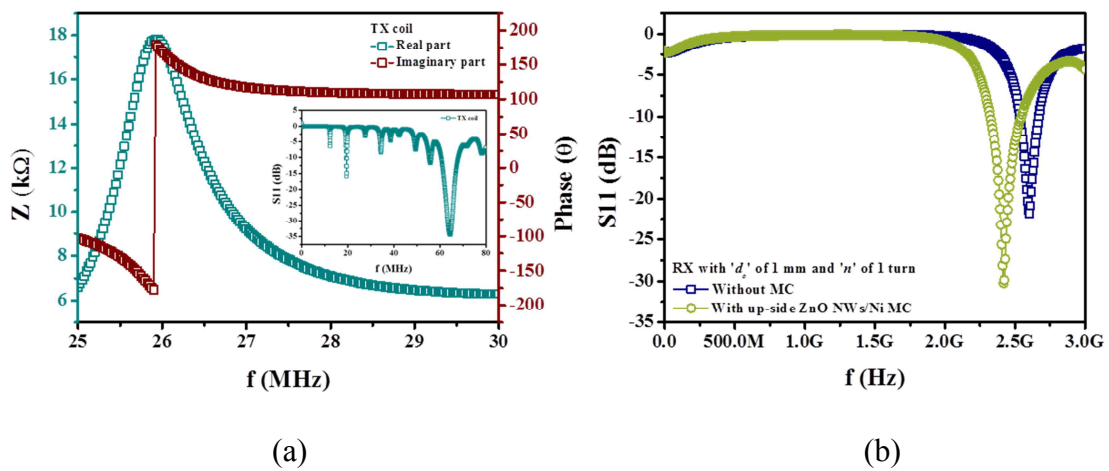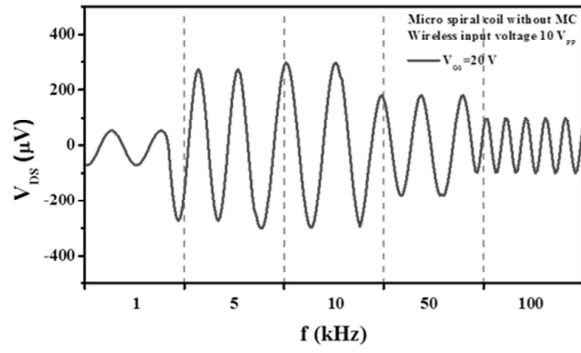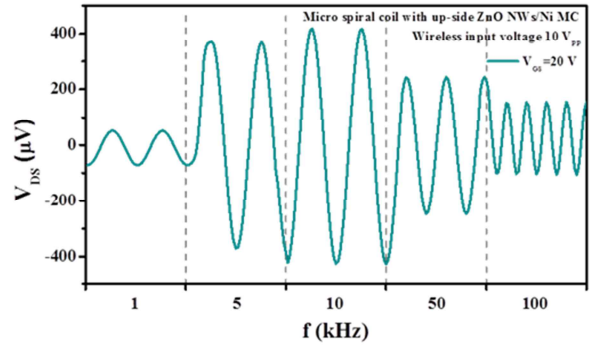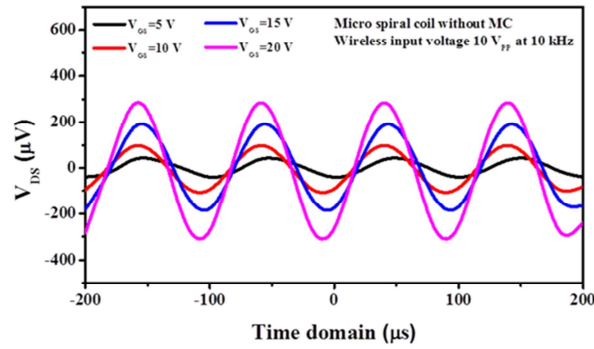

(a)   (b)

Fig 3.2.1 'f_{sr}' measurement of TX and RX coil antennas. (a) 'f_{sr}' of TX with macro size. (b) 'f_{sr}' of RX with micro size.
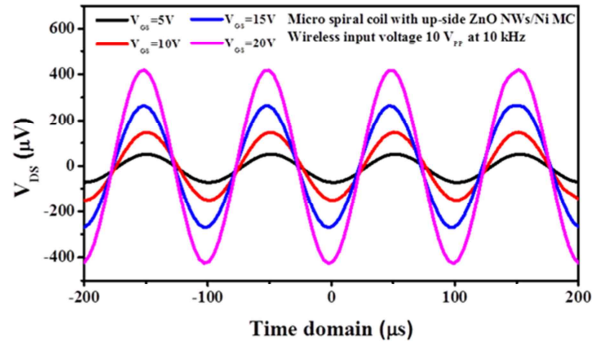
(a)

(b)

(c)

(d)

Fig 3.2.2 Electrical characteristics of wireless source-drain system of a-IGZO TFT. (a) Frequency characteristic of wireless a-IGZO TFT without MC. (b) Frequency characteristic of wireless a-IGZO TFT with up-side ZnO NWs/Ni MC. (c) AC transfer characteristic of wireless a-IGZO TFT without MC. (d) AC transfer characteristic of wireless a-IGZO TFT with up-side ZnO NWs/Ni MC.

Firstly, the frequency characteristic of wireless a-IGZO TFT was measured. The Applied frequency range were from 1 kHz to 100 kHz. From the results in Fig 3.2.2 (a) and (b), we can confirm that the WPT efficiencies of wireless a-IGZO TFTs are increased up to 10 kHz and the efficiencies are decreased as increasing the frequency. It can be explained that as the frequency is increased, the self-resonance frequency of coil is approached hence, the WPT efficiency of wireless a-IGZO TFT is increased however, the '$\mu_{FE(h)}$' and 'f_{max}' of α-IGZO

TFT faces the limitation so the WPT efficiency begins to be decreased. In these resons, the operating frequency with the highest performance of wireless α-IGZO TFT was observed at 10 kHz and the measured output 'V_{DS}' was 840 μV_{PP} at the case with the up-side ZnO NWs/Ni MC, which is higher than the case without the MC of 600 μV_{PP}. Secondly, the AC transfer characteristics of a-IGZO TFT with micro antenna according to the 'V_{GS}' as shown in Fig. 3.2.2 (c) and (d). In the same way with the prior measurement, the 'V_{GS}' were changed from 5 V to 20 V when the frequency was fixed at 10 kHz. From the results, for the AC electrical characteristics of source and drain in the wireless α-IGZO TFTs, the wireless AC signals are well controlled by the DC gate bias and the both results from frequency and AC transfer characteristics show the wireless α-IGZO TFT with the up-side ZnO NWs/Ni MC has the better performance than the case without the MC however, the WPT efficiency still remains low so it needs to be improved more.
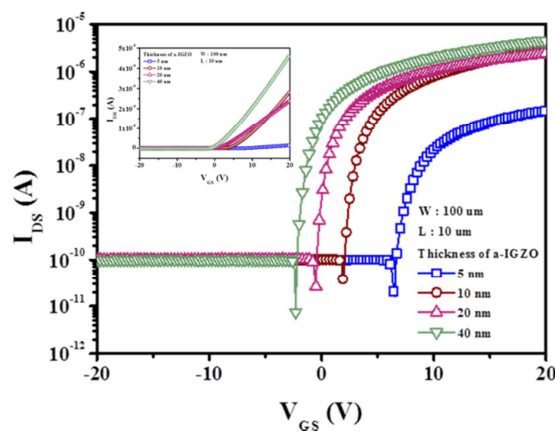
3.3 Improvement of α-IGZO TFT

Fig 3.3.1 Threshold shift according to thickness of a-IGZO channel.

There are two issues to apply the TFT to the wireless system, which 'V_{th}' needs to be close to '0' value and '$f_{m\,ax}$' should be increased. When the 'V_{th}' is close to '0' value, the TFT can be realized with better performance for switching. As controlling the thickness of α-IGZO channel layer, the threshold voltage close to '0' point could be obtained. When the thickness of α-IGZO is too thin, the resistance is increased hence, the proper thickness is required. The proper thickness was observed at 40 nm as shown the Fig. 3.3.1.

(a)

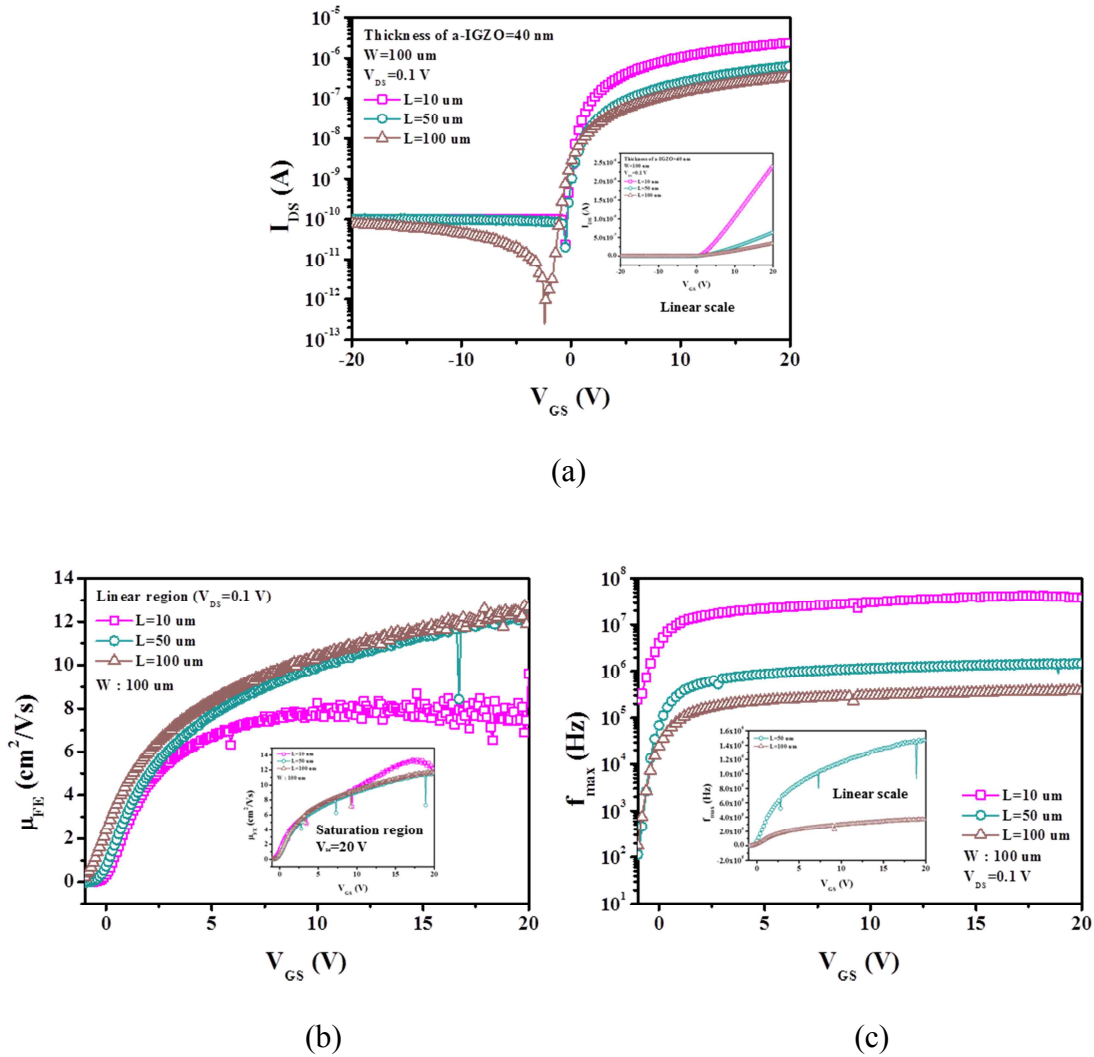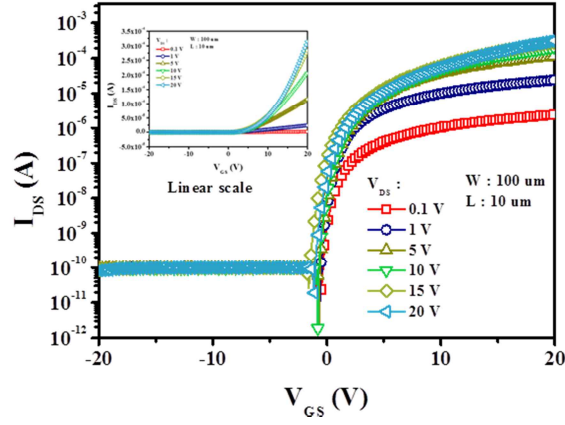(b)   (c)
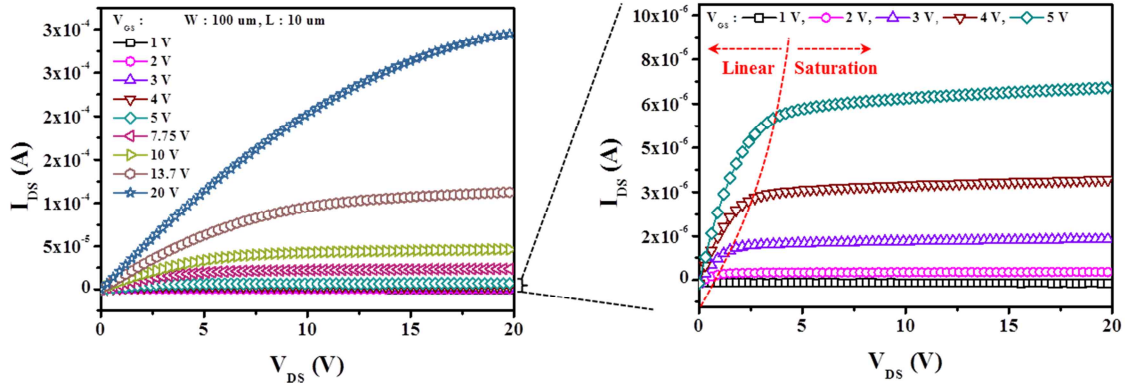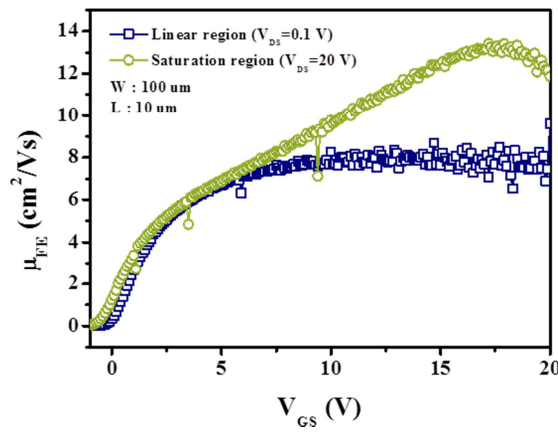
Fig 3.3.2 A-IGZO TFT characteristics according to channel length. (a) Transfer curve. (b) Saturation and linear mobility. (c) Cutoff frequency.

(a)

(b)

(c)

Fig 3.3.3 DC characteristics of α-IGZO TFT with 10 um of channel length. (a) Transfer curve. (b)

Output curve. (c) Linear and saturation mobility.

The thickness of α-IGZO was fixed as 40 nm and the transfer curve was obtained according to the channel length of α-IGZO layer to improve the mobility and cut-off frequency for satisfying the requirement of micro coil working. Fig. 3.3.2 shows the improvement of cutoff frequency of α-IGZO TFT. As the channel length is increased, the linear regime '$\mu_{FE(lin)}$' is enhanced. However, the saturation regime '$\mu_{FE(sat)}$' has different result that the case of '$L = 10\ um$' has the highest mobility value and cut-off frequency. It can be explained by 'early effect' that the slope is increased as the channel length becomes shorter in the saturation region and it leads to increase the saturation regime '$\mu_{FE(sat)}$'. The thickness of α-IGZO with the 'L' of $10\ um$ was selected due to the highest 'f_{max}' and Fig. 3.3.3 shows the DC characteristics of α-IGZO TFT with the 'L' of $10\ um$. In comparison to the previous α-IGZO design, the 'f_{max}' is increased from 1.5 MHz of previous work up to 10 MHz at 'V_{GS}' of 20 V.
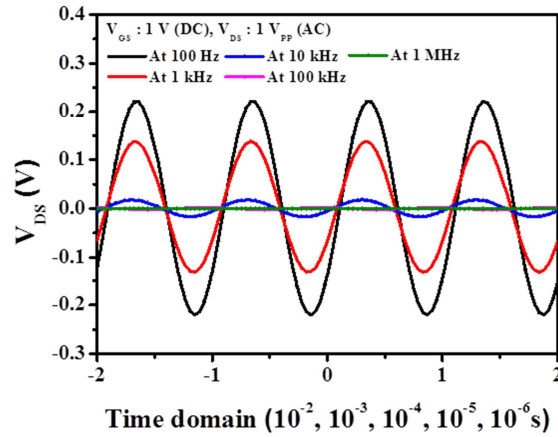

(a)

Fig 3.3.4 AC characteristic of α-IGZO TFT with 10 um of channel length. (a) AC characteristic at source-drain part of α-IGZO TFT according to frequency

To compare with the previous TFT design, AC characteristics of α-IGZO TFT were measured at the source-drain part of α-IGZO TFT in the same condition with previous measurement system, where the input DC '$V_{GS} = 1\,V$' and AC '$V_{DS} = 1\,V_{PP}$'. After improving the 'μ_{FE}' and the 'f_{max}', the output 'V_{DS}' was observed up to MHz range as shown in Fig 3.3.4 (a). The output 'V_{DS}' was signicantly increased in comparison with the previous work, which the limit transportation frequency from previous design was observed at 310 kHz. From the results, we could improve the frequency charcteristics of α-IGZO TFT.

3.4 Improvement of MC

To improve the WPT efficiency of spiral coil antenna, the various MC structures were designed and the inductance and WPT efficiency were mearued to compare their performance. Fig 3.4.1 shows the results the measured inductance and WPT efficiency. The spiral coil antenna with the 'd_o' of 1 mm were used and other parameters and the condition of measurement were same with the previous work. The inductance values of fabricated spiral coil antennas with various MC structures were measured by using test fixture connected with impedance analyzer. The highest inductance value was observed at the spiral coil antenna with the back-side ZnO NWs/Ni MC and the back-side MC structures have higher inductance than others. At the measurement of WPT efficiency, the spiral coil antenna with the back-side ZnO NWs/Ni MC has highest performance and ZnO NWs/Ni MC systems show the better performance than others. The difference of tendency from the results of inductance and WPT efficiency measurement is likely to be affected by unwanted parasitic resistance and quality fator.
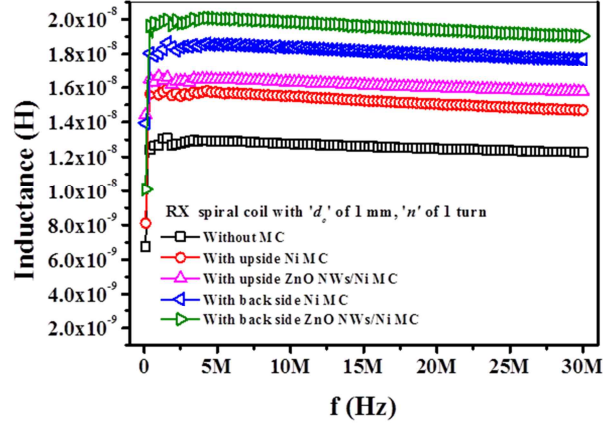
(a)
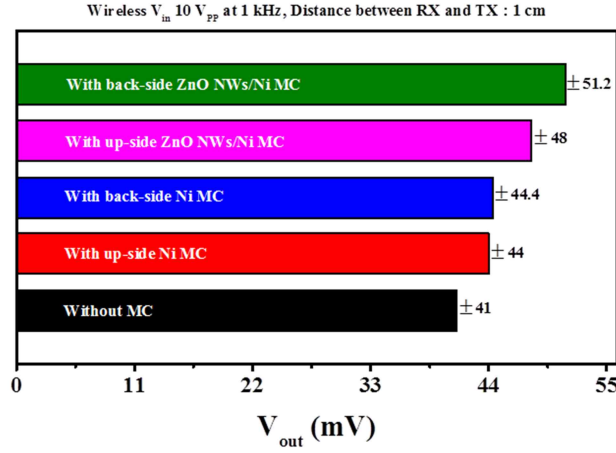
(b)

Fig 3.4.1 Inductance and WPT efficiency. (a) Inductance values according to MC designs. (b) WPT efficiencies according to MC designs.

3.5 Improvement of wireless source-drain system of α-IGZO TFT

After improving the WPT efficiency of spiral coil antenna and the cut-off frequency of α-IGZO TFT, the two systems were connected, which the source-drain and gate electrodes of α-IGZO TFT were individually connected with the spiral coil antenna with the back-side ZnO NWs MC structre and the characterisitics of wireless α-IGZO TFT were measured. Firstly, to confirm the performance of wireless system in the source-drain part of

α-IGZO TFT, the frequency and AC transfer characteristics of wireless a-IGZO TFT were measured in the same condition with the previous measurement of wireless a-IGZO TFT. We can confirm that the performance of wireless α-IGZO TFT is significantly enhanced in comparison with the previous work from the results in Fig 3.5.1 (a-b).

(a)   (b)
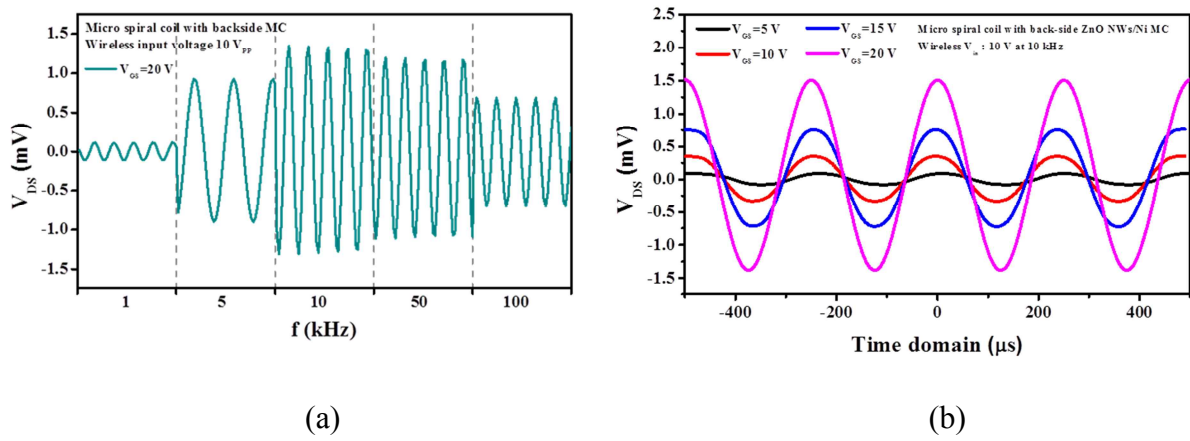
Fig 3.5.1 Improved electrical characteristics of wireless source-drain system of a-IGZO TFT. (a) Frequency characteristic with back-side ZnO NWs/Ni MC. (b) AC transfer characteristic with back-side ZnO NWs/Ni MC.

3.6 Characteristics of wireless gate system of α-IGZO TFT

To realize our concept, a gate part of TFT is also necessary to be applied by wireless system. For this reason, the wireless system was applied to the gate part of α-IGZO TFT, which the improved wireless system and α-IGZO TFT design were used. To apply the WPT system to the α-IGZO TFT, 'V_{GS}' needs to be rectified as a DC bias. Hence, the spiral coil was connected with a schottky diode in series for half-wave rectification and the capacitor with capacitance of 1 uF was connected with them to make the wave closer DC. The result of half-wave rectification is represented in Fig 3.6.1.
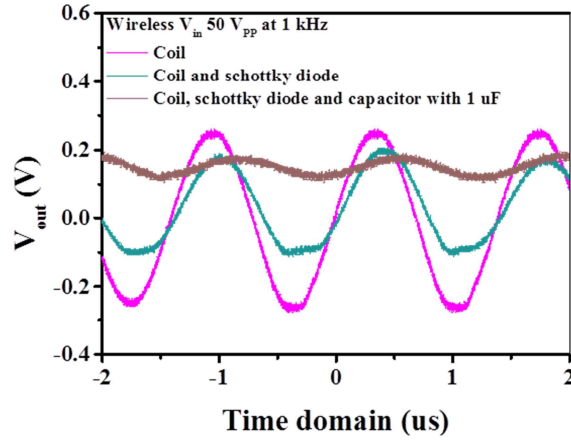
Fig 3.6.1 Characteristic of wireless rectification.

The WPT and rectification system were connected with the gate-source part of α-IGZO TFT, the wireless power was delivered by TX up to 100 V_{PP} at 1 kHz and the 'I_{DS}' was plotted according to the DC 'V_{DS}' sweep using Keithley semiconductor analyzer. The measured output and transfer characteristics show that the system is well operated as a transistor in Fig 3.6.2 (b) and (d), which the system can be used as a wireless switching or a rectifier. Fig 3.6.2 (a) and (c) show the output and transfer characteristics of α-IGZO TFT.
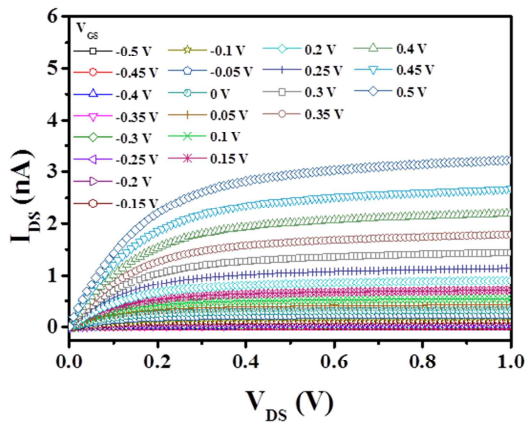
(a)
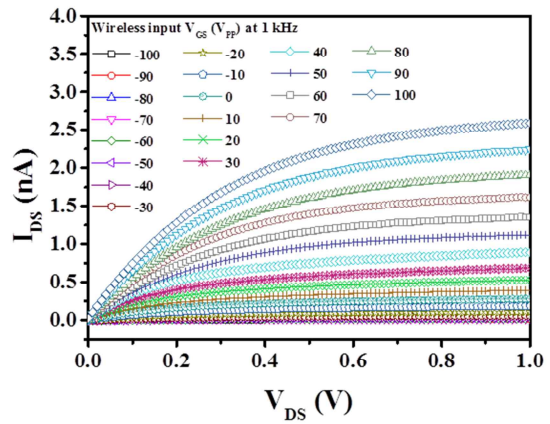
(b)
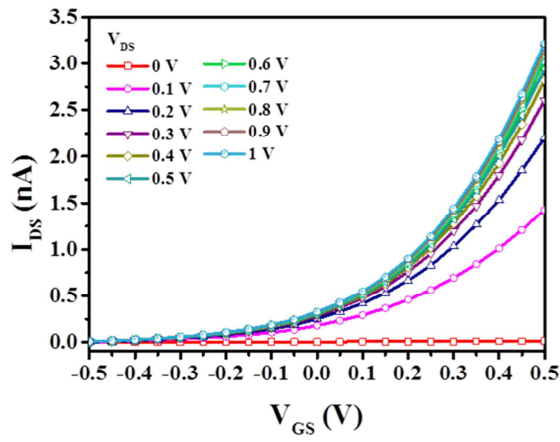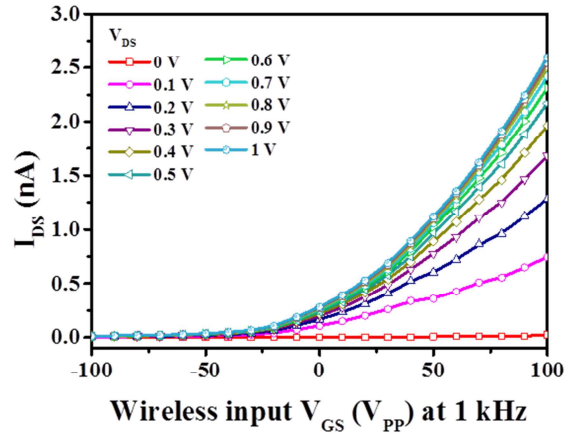
(c)   (d)

Fig 3.6.2 Electrical characteristics of wireless gate system of a-IGZO TFT. (a) Output characteristic

of a-IGZO TFT. (b) Output characteristic of wireless a-IGZO TFT with back-side ZnO NWs/Ni MC.

(c) Transfer characteristic of α-IGZO TFT. (d) Transfer characteristic of wireless a-IGZO TFT with

back-side ZnO NWs/Ni MC.

IV. **CONCLUSION**

We have studied micro WPT system to adopt α-IGZO TFT. Firstly, we confirmed that the wireless TFT system was well operated at source-drain part of TFT. However the wireless TFT system had low WPT efficiency hence the system was required to be improved. To enhance the wireless TFT system, we increased the operating frequency of α-IGZO TFT to satisfy the WPT efficiency increased as the operating frequency approaches the GHz level. Then the back-side Ni MC assisted by ZnO NWs was added in the center of spiral coil antenna structure to improve the WPT efficiency more. The fabricated designs were connected which the spiral coil antennas were connected with the source-drain and gate parts of α-IGZO TFT respectively. As a result, the efficiency of wireless TFT system at the source-drain part could be enhanced in comparison with the previous design. To realize the flexible and wearable system, a gate part of TFT is also necessary to be applied by wireless system. For this reason, the wireless system was applied to the gate part of α-IGZO TFT as well. The measured electrical characteristics showed that the system was well operated as wireless switching or rectifier. At this paper, optimization of WPT system was not performed thus the WPT efficiency was quite lower than the case applying power through wire. When the optimal parameters of TX and RX are set up according to distance between two coil antennas and frequency using simulators, the WPT efficiency can be significantly increased. Our purpose in this paper was to show the availability of wireless TFT concept for flexible and wearable system. From the experimental result, we could confirm that our wireless TFT concept have a high probability to substitute to the wire connection for wearable or flexible device issues.

References

[1] Casanova, Joaquin J., et al. Radio and Wireless Symposium, 2009. RWS'09. IEEE. IEEE, 2009.

[2] Webb, R. Chad, et al. "Ultrathin conformal devices for precise and continuous thermal characterization of human skin." Nature materials (2013).

[3] Kim, Dae-Hyeong, et al. "Materials and noncoplanar mesh designs for integrated circuits with linear elastic responses to extreme mechanical deformations." Proceedings of the National Academy of Sciences 105.48 (2008): 18675-18680.

[4] Qiang Wang and Hong Li. "Research on the wireless power transmission system based on coupled magnetic resonances." 2011 International Conference on Electronics Communications and Control (ICECC), 2011.

[5] David K. Cheng. Field and Wave Electromagnetics, Addison-Wesley, 1989, 703 pages.

[6] http://en.wikipedia.org/wiki/Wireless_power

[7] Shinohara, Naoki. "The wireless power transmission: inductive coupling, radio wave, and resonance coupling." Wiley Interdisciplinary Reviews: Energy and Environment 1.3 (2012): 337-346.

[8] Xie, Liguang, et al. "Wireless power transfer and applications to sensor networks." Wireless Communications, IEEE 20.4 (2013).

[9] Andre Kurs, Aristeidis Karalis, Robert Moffatt, J. D. Joannopoulos, Peter Fisher, and MarinSoljacic. "Wireless Power Transfer via Strongly Coupled Magnetic Resonances." *Science*, Vol 317, 2007.

[10] Brown, William C. "The history of power transmission by radio waves." Microwave Theory and Techniques, IEEE Transactions on 32.9 (1984): 1230-1242.

[11] Mohan, Sunderarajan S., et al. "Simple accurate expressions for planar spiral inductances." Solid-State Circuits, IEEE Journal of 34.10 (1999): 1419-1424.

[12] Jow, Uei-Ming, and Maysam Ghovanloo. "Design and optimization of printed spiral coils for efficient transcutaneous inductive power transmission." Biomedical Circuits and Systems, IEEE Transactions on 1.3 (2007): 193-202.

[13] Ghovanloo, Maysam, and Suresh Atluri. "A wide-band power-efficient inductive wireless link for implantable microelectronic devices using multiple carriers." Circuits and Systems I: Regular Papers, IEEE Transactions on 54.10 (2007): 2211-2221.

[14] Yoon-Ki Sin, Introduction to Electricity & Electronics, Kyobobook, 2009.

[15] Finkenzeller, Klaus. RFID handbook: radio-frequency identification fundamentals and applications. New York: Wiley, 1999.

[16] Gamet, E., et al. "Simulation of the contribution of magnetic films on planar inductors characteristics." Journal of magnetism and magnetic materials 288 (2005): 121-129.

[17] Yamaguchi, M., et al. "Analysis of the inductance and the stray capacitance of the dry-etched micro inductors." Magnetics, IEEE Transactions on 27.6 (1991): 5274-5276.

[18] Mukerji, Saurabh Kumar, et al. "Eddy currents in solid rectangular cores." Progress In Electromagnetics Research B 7 (2008): 117-131.

[19] Kazimierczuk, Marian K. High-frequency magnetic components. John Wiley & Sons, 2013.

[20] Park, Joon Seok, et al. "Review of recent developments in amorphous oxide semiconductor thin-film transistor devices." Thin Solid Films 520.6 (2012): 1679-1693.

[21] Nomura, Kenji, et al. "Amorphous oxide semiconductors for high-performance flexible thin-film transistors." Japanese journal of applied physics 45.5S (2006): 4303.

[22] Pierret, Robert F. "Semiconductor device fundamentals." (1996).

[23] http://en.wikipedia.org/wiki/Indium_gallium_zinc_oxide

[24] Nomura, Kenji, et al. "Room-temperature fabrication of transparent flexible thin-film transistors using amorphous oxide semiconductors." Nature 432.7016 (2004): 488-492.

[25] Sugunan Abhilash, et al. "Zinc oxide nanowires in chemical bath on seeded substrates: role of hexamine." Journal of Sol-Gel Science and Technology, 2006, pp. 49-56.

[26] Kim Hyunjin, et al. "Enhancement of piezoelectricity via electrostatic effects on a textile platform." Energy & Environmental Science, 2012, pp. 8932-8936.

[27] Jung Inn Sohn, et al. "Engineering of efficiency limiting free carriers and an interfacial energy barrier for an enhancing piezoelectric generation." Energy & Environmental Science, 20132, pp. 97-104.

[28] Xu, Sheng, et al. "Patterned growth of vertically aligned ZnO nanowire arrays on inorganic substrates at low temperature without catalyst." Journal of the American Chemical Society, 2008.

[29] Seung Nam Cha, et al. "Sound-Driven Piezoelectric Nanowire-Based Nanogenerators." Advanced Materials, 2010.

[30] Lee, Jae Sang, et al. "High-performance a-IGZO TFT with gate dielectric fabricated at room temperature." Electron Device Letters, IEEE 31.3 (2010): 225-227.

[31] Jeong, Jaewook, et al. "Scaling behaviour of a-IGZO TFTs with transparent a-IZO source/drain electrodes." Journal of Physics D: Applied Physics 45.13 (2012): 135103.

요 약 문

마이크로 안테나를 가지는 자기 유도 결합 방식 무선 박막트랜지스터 시스템 연구

본 연구는 기존의 기술한계를 극복하기 위한 새로운 방식의 플렉서블 및 웨어러블 디바이스 시스템 구현방식을 제안한다. 현재 바이오센서와 같은 융합기술에 대한 관심이 고조됨에 따라 생체적합성을 위한 플렉서블 및 웨어러블 시스템이 크게 대두되고 있다. 일반적으로 구부릴 수 있는 전자재료와 유연한 형태를 가지는 소자를 구현하는 방식의 연구가 다른 연구진들에 의해 활발히 진행되고 있다. 실제 플렉서블 및 웨어러블 시스템을 구성하는 소자의 크기는 전체 시스템에 비해 매우 작기 때문에 실제 시스템이 휘어질 때 발생하는 스트레스는 각 소자에 큰 영향을 미치지 않는다 하지만 각 소자의 신호나 전력 전달을 위한 와이어 연결은 전체 시스템의 크기에 비례하여 사이즈가 증가하기 때문에 큰 영향을 받게 되어 쉽게 끊어지게 된다. 문제의 근원이 되는 와이어 연결을 최소화시킨다면, 이 문제점을 효과적으로 해결할 수 있을 것이다. 본 연구는 와이어 연결을 최소화 시키기 위해 무선전력전송개념을 도입하여 새로운 방식의 플렉서블 및 웨어러블 시스템 구현에 대한 가능성을 살펴보고자 한다. 제안된 시스템 구현을 위해 무선전력전송 시스템을 전자소자의 핵심이 되는 트랜지스터와 연결하여 동작특성을 살펴보았다. 무선으로 전력 또는 신호를 수신할 수 있는 안테나를 트랜지스터에 적용시키기 위해서는 안테나 사이즈가 마이크로 레벨로 축소되는 것이 필요하고 플렉서블 및 웨어러블 시스템에 트랜지스터를 구현하기 위해서는 박막트랜지스터 구조가 적합하다. 먼저 안테나의 사이즈가 축소됨에 따라 감소되는 전송효율을 보상하기 위해 산화아연 나노구조체와 강자체 물질인 니켈을 이용한 자심을 안테나 중심에 적용시켜 그 효율을 증가시켰다. 또한 높은 자기공진주파수를 가지는 마이크로 안테나의 동작주파수를 맞추기 위해 높은 모빌리티 특성을 가지는 비정질 인듐갈륨산화아연 박막트랜지스를 제작하고 박막트랜지스터의 채널길이와 두께를 조정함으로서 차단주파수를 높일 수 있었다. 다음으로 제작된 마이크로 안테나와 박막트랜지스를 연결하여 그 특성을 분석한 결과 무선스위치와 정류기로서의 가능성을 파악할 수 있었다. 본 연구는 새로운 플렉서블 및 웨어러블 시스템 구현방식을 제시하였다는 점에 대해서 의의를 가진다.

핵심어: 무선 전력전송, 박막트랜지스터, 무선 박막트랜지스터

감사의 글

설레임을 안고 학교 정문을 들어선지 엊그제 같은데 어느덧 2 년이라는 시간이 흘러 졸업을 앞두게 되었습니다. 철부지였던 제가 이렇게 작은 열매 하나를 맺게 되면서 이 자리에 서기까지 많은 분들에 도움이 있었다는 것을 이제서야 깨닫게 되었습니다. 감사의 말을 드리고 싶은 분들이 너무 많고 감사의 마음을 글로 다 표현하기에는 제 글솜씨가 한없이 부족하지만 조금이나마 몇 글자 올려보겠습니다.

먼저 한없이 부족한 저에게 연구자로서의 지식과 소양을 채워주신 장재은 지도교수님께 감사의 말을 전하고 싶습니다. 매번 머뭇거리며 길을 헤매일 때 올바른 길로 인도해 주시며 조언을 아끼지 않으셨던 교수님께 진심으로 감사드립니다. 무엇보다도 언제나 변함없이 열정과 관심으로 저희를 대해주시는 교수님을 만났다는 것에 대해 제가 정말 운이 좋은 사람이란 생각이 들고 교수님의 관심과 열정 덕에 무사히 석사과정을 마칠 수 있었던 것 같습니다. 지도교수님과 더불어 바쁘신 와중에도 불구하고 학위논문 심사를 맡아주시고 지도해주신 로봇공학과 최홍수 교수님과 정보통신융합공학과 최지웅 교수님께 감사의 마음을 전하고 싶습니다. 최홍수 교수님께서 조언해주신 앞으로의 연구방향과 최지웅 교수님께서 지적해주신 현재의 연구방향은 앞으로 연구하는 데 있어 큰 나침반이 될 수 있을것이라 봅니다. 회로에 관한 상담을 언제나 친절히 답해주셨던 재민규 교수님께도 감사의 말씀을 전하고 싶고 입학 면접에서 진심어린 마음으로 많은 조언을 해주셨던 권욱현 석좌교수님께도 감사의 마음을 전하고 싶습니다. 또한 제가 이자리까지 설수 있도록 도움을 주신 손상혁 전공책임교수님, 박태준 교수님, 은용순 교수님, 박경준 교수님, 김민수 교수님, 최지환 교수님, 황재윤교수님께도 감사의 말씀을 전하고 싶습니다.

그리고 무엇보다도 저를 세상에 있게 만들어주시고 저에게 가장 소중한 가족, 친척들분께 감사의 말을 전하고 싶습니다. 항상 저를 믿어주시고 자신보다도 저를 먼저 생각해주시는 아버지, 어머니, 어려운일이 있을 때 먼저 나서서 해결해 주고 힘이 되어주는 형에게 항상 감사한 마음을 가집니다.

석사과정 동안 가장 많은 시간을 같이 보낸 연구실 식구들에게도 감사의 마음을 표합니다. 먼저 장비사용과 실험에 대해 많은 부분을 가르쳐 주시고 도와주신 박막트랜지스터의 달인 지나 아버님 광준이 형님, 나노홀의 달인 조기헬스회 회장님 승욱 선배, 탄소나노튜브의 달인 교수님의 분신 정희 선배, 그래핀에 달인 고스트 재훈이, 동기로써 많은 힘이 되어 주는 나노와이어의 달인 캐치볼 민경이, 실험을 많이 보조해주고 연구실 막내로서 고생이 많은 현빈 닮은 조류학자 류민규 후배님, 연구실에서 제일 이쁜 홍일점 이경화 후배님, 그리고 곧 결혼 예정인 재한이 형, 국방과학연구소에서 열심히 무기 개발 중인 나의 사수 종구, 삼성에서 고생이 많은 예리 선배, 모두에게 감사의 말을 전합니다. 또한 학부과정 연구실에서도 저에게 많은 도움을 주신 경훈이 형님, 주용이 형님, 강현이 형님, 동균이 형님, 송진이 형님, 효섭이, 성준이, 윤석이, 원경이에게도 감사의 말을 전하고 싶습니다.

비록 글로써 전부 언급하지는 못했지만, 오랫동안 지지고 볶으면서 어려움을 함께 헤쳐나갔던 소중한 친구들, 동기들, 선후배님들, 주변분들 모두 감사드립니다. 앞으로 저도 여러분께 힘이 될 수 있는 존재가 될 수 있도록 노력하겠습니다.